Multiscale spectral discrimination of poorly crystalline and intermixed alteration phases using aerial and ground-based ExoMars rover emulator data

E.J. Allender [a,b,*], C.R. Cousins [a], M.D. Gunn [b], E.R. Mare [a]

[a] *University of St Andrews, School of Earth and Environmental Sciences, Irvine Building, St Andrews KY16 9AL, UK*
[b] *Aberystwyth University, Department of Physics, Penglais Campus, Aberystwyth SY23 3BZ, UK*

ARTICLE INFO

Keywords:
ExoMars
PanCam
Spectral
Multiscale
Mineralogy

ABSTRACT

A key goal of the ExoMars rover *Rosalind Franklin* is to analyze accessible hydrated mineral deposits using panoramic multiscale and multispectral imagery. We conducted a multiscale spectroscopic study on hydrothermally-altered basalt-hosted soils in the geothermal area of Námafjall in northern Iceland. Basaltic lavas here that have experienced first-order geochemical alteration produce a variety of cm-to-meter scale poorly crystalline alteration patterns. The resulting unconsolidated sediments provide a natural analogue material to investigate intimately mixed soils comprising multiple poorly crystalline hydrated phases. We use emulator instruments which replicate the capabilities of the ExoMars 2022 Panoramic Camera (PanCam), the Infrared Spectrometer for ExoMars (ISEM), and the CLose-UP Imager (CLUPI), alongside Raman, aerial, and X-Ray Fluorescence spectroscopic data to investigate how the detection of these mixed basalt-derived alteration phases varies as a function of spatial and spectral scale. We find soils at our study site to be comprised of unconsolidated sediments including Al-OH minerals, hydrated silica, and a variety of ferric oxides, all of which *Rosalind Franklin* will likely encounter along its traverse at Oxia Planum. We report on (i) the synergy and limitations between Mars rover instrument emulators as an integral part of mission preparation, (ii) how the mixed nature of these hydrothermally-altered soils affects resulting mineralogical interpretations at multiple scales, and (iii) geochemical inferences that can be made using ExoMars 2022 imaging emulators.

1. Introduction

Mars surface exploration relies upon the cross-referencing of multi-scale observations provided by orbiters and landed spacecraft, with the latter providing a local measure of ground truth to regional-scale orbital images. In 2022, the European Space Agency (ESA) and Roscosmos will launch the ExoMars 2022 rover *Rosalind Franklin* and its surface platform *Kazachok*. A primary objective of the ExoMars mission is to detect evidence of extinct life within subsurface deposits – chiefly organic biomarkers (Vago et al., 2017). If present, these are more likely to be found in environments indicative of water-rock interaction, and in minerals that can reduce the damaging effects of UV-induced photochemical reactions and ionizing radiation (dos Santos et al., 2016; Vago et al., 2017; Laurent et al., 2019). *Rosalind Franklin* will land within a 100 km landing ellipse in Oxia Planum, a Noachian-aged (>3.8 Ga) plain

which is located between the ancient terrain of Arabia Terra and the lower-lying basin of Chryse Planitia (Fawdon et al., 2020). Elevations within the ellipse range from −2600 m to −3100 m and there is very low local surface relief (The ExoMars 2018 Landing Site Selection Working Group, 2014). As such, spectral discrimination of units will be integral to establishing the stratigraphic context to any detailed investigations. The landing ellipse itself contains an Al and Fe/Mg phyllosilicate-rich basal unit overlain by a younger deltaic sedimentary fan – indicative of the ponding of water post-dating the layered formation (Quantin-Nataf et al., 2018). Later stage volcanic activity has partially covered the layered clay deposits, resulting in a dark, mafic, resistant unit that is projected to be Amazonian (<3 Ga) in age. The entire region has been heavily eroded since these units were emplaced, resulting in the formation of isolated buttes exposing the underlying Noachian rock (The ExoMars 2018 Landing Site Selection Working Group, 2014; Fawdon

et al., 2020; McNeil et al., 2020). As a consequence, *Rosalind Franklin* will likely encounter low-relief hydrated Al/Fe/Mg-OH bearing mineral terrains along its traverse, as well as sedimentary and igneous deposits.

Rosalind Franklin carries the Panoramic Camera (PanCam) instrument, which will provide local scale morphological and mineralogical context along its traverse (Coates et al., 2017). PanCam is composed of two wide angle cameras (WAC) set 50 cm apart along an optical bench. Each WAC images a 38.3° field of view (FOV) and contains an 11-space filter wheel comprised of three broadband color filters, six narrowband geology filters, and two solar filters. The wavelength range captured by PanCam spans 440–1000 nm. PanCam RGB imaging differs from that of Mastcam (Malin et al., 2010) (onboard NASAs MSL rover *Curiosity*) and Mastcam-Z (Bell et al., 2016) (onboard NASAs Mars2020 rover *Perseverance*) in that PanCam makes use of broadband color filters instead of RGB Bayer filters (Wellington et al., 2017; Bell et al., 2016). When operating in concert with the Infrared Spectrometer for ExoMars (ISEM) (Section 2.2.2), their combined wavelength range will span 440–3300 nm, enabling absorption features consistent with hydrated mineralogy to be analyzed for targets in the FOV of PanCam. This range also provides a means to effectively ground-truth orbital observations of hydrated materials.

Multiple rover missions (e.g. NASAs *Curiosity* and *Spirit*) have previously encountered sediments containing mixtures of crystalline minerals with a significant x-ray amorphous component – comprising phases including volcanic glass, nanophase ferric oxides, opaline silica, and amorphous sulfates (Squyres et al., 2008; McSween Jr. et al., 2010; Rice et al., 2010; Bish et al., 2013; Vaniman et al., 2014; Dehouck et al., 2014). Hydrated (opaline) silica is a common alteration product through aqueous alteration with basalt and has been detected in several localities on Mars in both orbital (Sun and Milliken, 2018; Tarnas et al., 2019) and ground-based measurements (Squyres et al., 2008; Rice et al., 2010). It is therefore likely the ExoMars rover *Rosalind Franklin* will encounter sediments bearing similar amorphous phases at Oxia Planum, intermixed with more crystalline phases such as Al- and Fe/Mg-bearing phyllosilicates (Quantin-Nataf et al., 2018). Unlike *Curiosity*, *Rosalind Franklin* does not have X-Ray Diffraction (XRD) analytical capability; sediment mineralogy will be inferred from ground-level visible to near-infrared (VNIR) to shortwave-infrared (SWIR) reflectance spectral measurements and Raman spectroscopy in combination with orbital remote sensing data and sedimentological context. However, features observed at ground-level are inherently more complex than what can be observed remotely from orbit. Ground-level remote-sensing data is also challenged by intimate, micron-scale mixtures of minerals, often found in geologic settings. VNIR to SWIR spectral data can be heavily influenced by minor phases that exhibit strong electronic or vibrational absorption features, providing an inaccurate assessment of the bulk mineralogy of a target region, whether at > 1 m scale or < 1 cm scale (Poulet et al., 2008; Cuadros et al., 2019).

In this work, we build upon a study by Carson (2015) who investigated hydrothermal acid-sulfate alteration in North-Eastern Iceland at micro- and nano-scales using XRD, X-Ray Fluorescence (XRF), Scanning Electron Microscope (SEM) and aqueous geochemistry techniques. We use a Mars-analog field site at Námafjall in Iceland to investigate highly localized hydrated mineral suites resulting from basaltic alteration at multiple spatial scales (spanning meters to microns) using instrument emulators representing the imaging and remote spectroscopic instruments on board the ExoMars rover. Investigating the synergy and limitations between Mars rover instruments is an integral part of mission preparation and includes the deployment of instrument emulators for NASA Mars2020 (Martin et al., 2020) and ESA ExoMars (Harris et al., 2015; Allender et al., 2020) at Mars-analog field sites. In this work we investigate the capabilities of our ExoMars emulator suite, discuss the difficulties associated with the detection of spatially mixed hydrated materials across meter-to-micron scales, and illustrate how their mixed nature can affect mineralogical interpretations and resulting geochemical inferences.

1.1. Field site

We explore the inter-operability of the ExoMars remote-sensing emulator suite at a Mars-analog site in North-Eastern Iceland (65°38′26.5″N, 16°48′43.2″W, see Fig. 1). The Hverir geothermal field at Námafjall contains multiple inactive argillic alteration haloes embedded within subaerial basaltic lavas. Visible alteration gradients extend radially from extinct fumarole centers, and vary in size from 2 to 25 m. While such extreme alteration gradients are not expected at ExoMars' landing site at Oxia Planum, which is likely an ancient fluvio-lacustrine environment, our emulators were tested on these features because they showcase distinct stages of temperature dependent alteration within a reasonably small area, providing an ideal test-case to investigate the small to large-scale alteration of basalt to secondary hydrated and poorly crystalline phases. For our test site, we selected a trio of extinct fumaroles which were easily identifiable from both aerial and ground-based imagery and sampled across these in an NW-SE direction (Fig. 1-C:G). Furthermore, this field site has: (i) scant vegetation coverage (ii) well-characterized geology and (iii) access to mains power for the purposes of field-testing the ExoMars emulator suite.

2. Methods

2.1. Aerial data

A collection of orbital imagery covering the Oxia Planum landing ellipse has been synthesized over the past decade. Hyperspectral data [400–3920 nm] from NASAs Mars Reconnaissance Orbiter (MRO) Compact Reconnaissance Imaging Spectrometer for Mars (CRISM) instrument has allowed mineralogical maps to be created at 18 m/pixel resolution for targeted surface features (Murchie et al., 2009). In addition, high-resolution color and near-infrared imagery has been collected at the orbital scale by MROs High Resolution Imaging Science Experiment (HiRISE) [400–1000 nm at 25 cm/pixel] and Context Camera (CTX) [500–800 nm at 6 m/pixel], ESAs Mars Express High Resolution Stereo Camera (HRSC) [440–970 nm at 2 m/pixel] and Trace Gas Orbiter (TGO) Color and Stereo Surface Imaging System (CaSSIS) [480–985 at 5 m/pixel].

To emulate this meter-scale hyperspectral coverage we obtained aerial datasets from the archived dataset IPY07–09 acquired by the NERC Airborne Research and Survey Facility (ARSF), courtesy of the NERC Earth Observation Data Centre. This aerial data was collected using two hyperspectral sensors operated by ARSF at the time of data collection in September 2008. The Eagle VNIR hyperspectral sensor collects data at a spectral resolution of 2.9 mm across the 400–970 nm wavelength range while the Hawk sensor extends this range into the infrared, spanning 970–2450 nm at a spectral resolution of 8 nm. Eagle and Hawk both have a spatial resolution of 2 m/pixel. ARSF Eagle and Hawk data were supplied in georeferenced 'radiance at sensor' (processing level L3a) format. In order to generate ground reflectance values this data was corrected for atmospheric effects using the FLAASH module in Harris Geospatial ENVI 5.4 in combination with a 2 m/pixel LIDAR Digital Elevation Model (DEM) provided with the dataset. The corrected Eagle and Hawk datasets were then joined across their common 970 nm bands and wavelength regions affected by significant atmospheric and surface H_2O were removed prior to display. Spectral regions of interest containing ~ 50 pixels ($\sim 20 \times 10$ m on the ground) were taken over (i) the fumarole trio [red], (ii) in a grass field [green], (iii) from the bare road surface [grey], and (iv) from the bare soil [brown] in the Námafjall region to compare their responses in the SWIR (Figs. 1-E and 2).
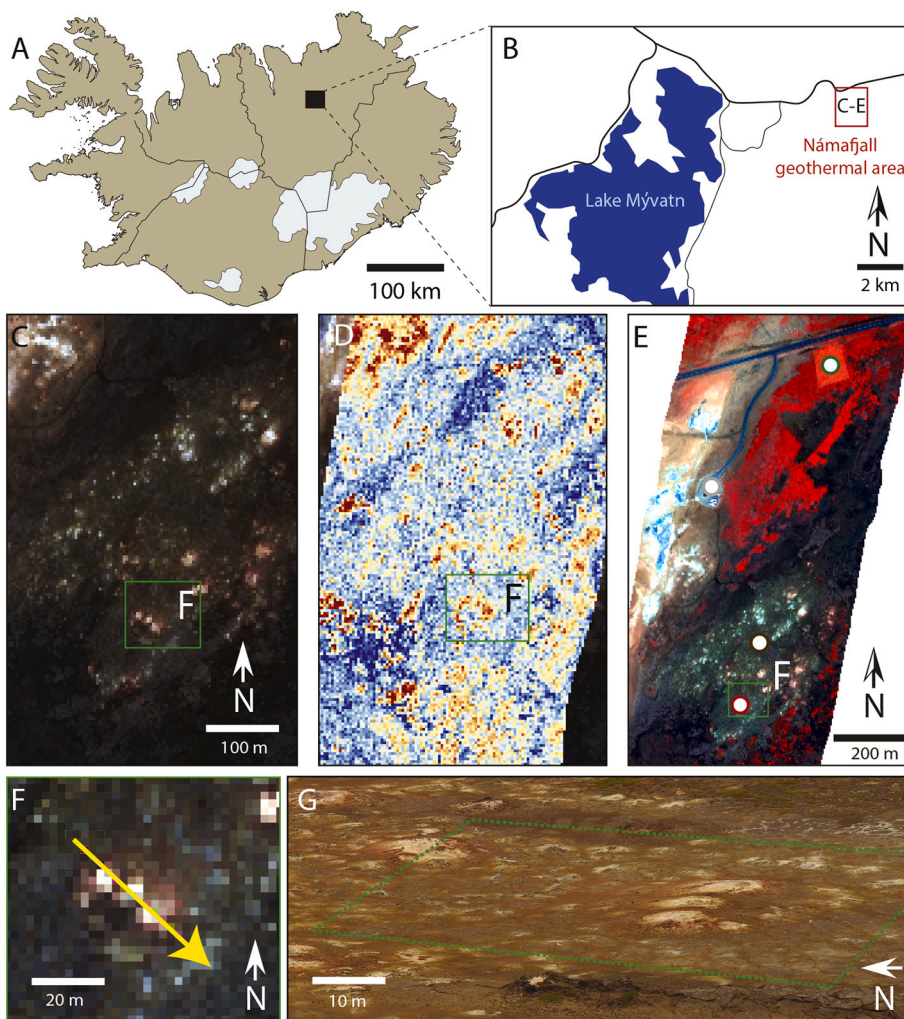
Fig. 1. A: Location of the field site in Iceland. Greyed areas are glaciers. B: Locator map for the Námafjall geothermal area, in which the Hverir fumarole field is located. C: Eagle RGB image of Námafjall, with the fumarole trio highlighted in the inset. D: Eagle RGB image overlain with Hawk false color map of reflectance at 2203 nm – red pixels have higher reflectance and highlight fumaroles. E: Eagle RGB image overlain with vegetation index (red is healthy vegetation) showing the regions of interest where aerial spectra were extracted for Fig. 2. F: Eagle RGB of fumarole trio test-site, overlain with NW-SE transect direction. G: Context field image of the fumarole trio taken facing east on the summit of Námaskarð. The area in green corresponds to the area in F. (For interpretation of the references to color in this figure legend, the reader is referred to the web version of this article.)
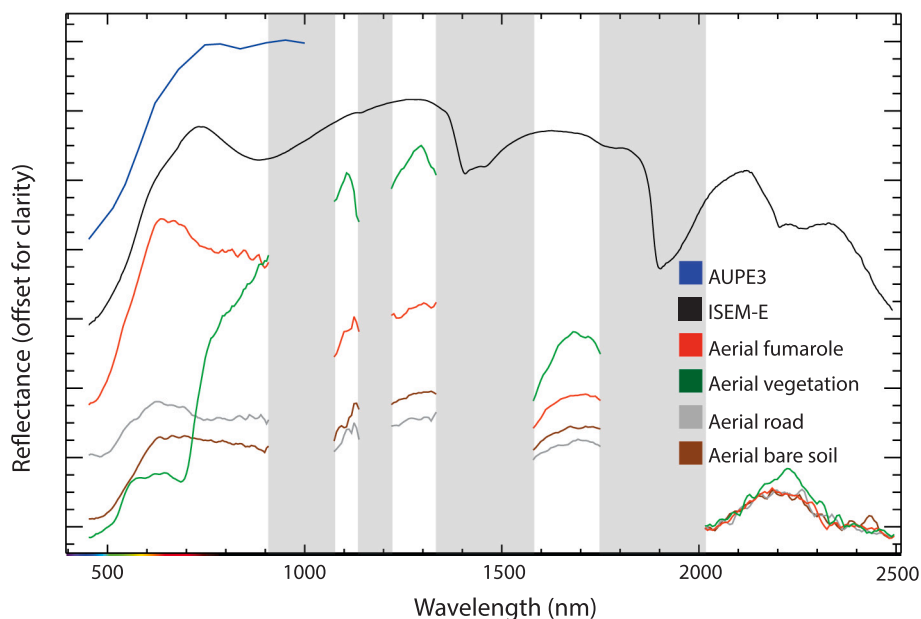

Fig. 2. Mean AUPE3, ISEM-E and aerial spectra spanning the fumarole trio. Additional aerial spectra from vegetation, road surfaces, and bare soil (ROIs marked in Fig. 1-E) illustrate that the large overlapping feature at ~1900 nm masks true absorptions in the ~2200 nm region (Knadel et al., 2014). Oversaturated H_2O absorption regions have been removed from the aerial spectra. We see good agreement between AUPE3 and ISEM-E observations in the VNIR.

2.2. Ground-based data

2.2.1. PanCam and the Aberystwyth University PanCam Emulator 3 (AUPE3)

PanCam emulator data is provided by the Aberystwyth University PanCam Emulator 3 (AUPE3), built with off-the-shelf components to replicate the specifications of ExoMars PanCam as closely as possible, including being mounted on an optical bench 2 m above the ground to replicate its height on *Rosalind Franklin's* mast (Harris et al., 2015; Allender et al., 2020). The AUPE3 WAC FOV is 34°, slightly smaller than that of PanCam (38.3°), and in place of the PanCam solar filters in positions 10 and 11 there is a luminance filter covering the visible portion of the spectrum and an empty filter slot for panchromatic imaging (Harris et al., 2015). Details of the filter wheels in Left WAC (LWAC) and Right WAC (RWAC) cameras for AUPE3 versus the ExoMars PanCam are provided in Table A1 in the Supplement. While the spectral 'geology' filter center wavelengths and bandpasses differ between ExoMars PanCam and MER Pancam (Cousins et al., 2012), PanCam data analysis builds on a wealth of existing data regarding image processing from both flight and emulator instruments (e.g. Alexander et al., 2006; Bell et al., 2004, 2004b, 2004c; Farrand et al., 2006, 2008, 2013, 2014; Barnes et al., 2011a; Barnes et al., 2011b; Parente et al., 2009).

AUPE3 was deployed at a working distance of 4 m from the midpoint of the fumarole trio. At this distance, its spatial resolution was 2.4 mm/pixel. Vertical overlap between LWAC and RWAC images was set to 61% and horizontal overlap was 30%. Weather conditions were overcast at the time of data collection, resulting in uniform lighting conditions. A MacBeth ColorChecker was placed in front of the center fumarole to enable radiometric calibration post-imaging. We assume both the MacBeth ColorChecker and the outcrop surface are Lambertian scatterers and, to ensure both were imaged under the same illumination conditions with the same geometry and at approximately the same time, the Macbeth ColorChecker was positioned such that it had approximately the same local incidence/emission angles as the targeted features. We therefore do not consider corrections for diffuse vs direct illumination. All raw images were processed to R* reflectance (defined by Reid et al. (1999)) using the ExoMars Spectral Analysis Tool (ExoSpec) developed by Allender et al. (2018). ExoSpec performs flat-fielding, radiometric correction, and correction from radiance to R* reflectance using the in-scene Macbeth ColorChecker.

To investigate local, sub-meter mineralogical variation 14 regions of interest (ROI) containing approximately 36 pixels in AUPE3 image data (~1.5 cm by ~1.5 cm) were created in the shared overlap between LWAC and RWAC images along the NW-SE transect line (Figs. 4-A and 5-B). These ROI were selected so that they overlapped with point spectra collected in the field by the ISEM emulator (ISEM-E) in handheld mode (Section 2.2.2). We performed principal component analysis (PCA) with these ROI to visualize and identify spectra that possess unique characteristics with respect to the entire dataset. Before PCA processing AUPE3 transect spectra were normalized to unit length so as to compare differences in spectral shape while minimizing albedo differences.

Each endmember in our reference library is labeled with its NASA Reflectance Spectroscopy Laboratory (RELAB) reference number and was chosen based on recent geological studies of the Námafjall region (Carson, 2015; Harris et al., 2015). To estimate endmember contributions for each target we resampled a subset of spectra from the RELAB database (See Supplementary Information) to AUPE3 wavelengths and performed spectral feature fitting using the Monte Carlo Markov Chain (MCMC) fitting routine developed by King and Fletcher (2020). This fitting routine uses an underlying linear mixing model – each "fitted" spectrum is calculated using a linear sum of endmembers weighted by their estimated percentage contribution. There are several advantages to using this MCMC technique with spectral data: (i) it allows uncertainties on endmember contributions to be estimated, (ii) it allows the endmember parameter space to be thoroughly explored and (iii) the results of MCMC are relatively easy to understand – though as with any

statistical analysis care must be taken when making inferences from its output. However, the main caveat to our MCMC approach is that the percentage contributions it provides are not true quantitative abundances. Rather, these contributions contain biases that arise from applying a linear mixing model to reflectance data that constitutes a non-linear mixture of light scattered at the mineral grain-level. Other studies (i.e. Lapotre et al. (2017)) recommend reflectance data be converted to single-scattering albedo and optical constants for endmember constituents be derived to address non-linearity issues at the grain-level; they use an alternative MCMC implementation to quantify errors and uncertainties associated with obtaining quantitative abundances from intimately mixed spectral data.

It is important to note that, in general, there is a negative relationship between grain size and reflectance. Increasing the grain size will decrease the overall reflectance of the spectrum but increase absorption band strength to the point of band saturation, after which reflectance strength will decrease (Clark, 1999; Van Keulen et al., 2000). The positions of observed absorption features are not affected. Soils observed in the field by AUPE3 consisted of mixed grains in the range of 100–500 μm and were interspersed with larger float rocks. Grain size measurements of reference library spectra were not provided in the RELAB database; we therefore expect there will be some differences in grain sizes between our reference library spectra and the spectra observed in the field by AUPE3 which will affect the quality of matching in the MCMC fitting procedure.

To estimate image spectral diversity we performed image classification using endmembers extracted from the 6-band AUPE3 LWAC image. To create the endmember reference library we performed a minimum noise fraction (MNF) rotation and created regions of interest within the resulting bands containing spatially coherent information. The four ROI endmembers selected represented "shade", "light soils", "red soils", and "yellowed soils". Supervised classification was then performed using the Spectral Angle Mapper (SAM) metric (Kruse et al., 1993). SAM treats each pixel and endmember spectrum as an n-dimensional vector in n-dimensional parameter space (where n is the number of bands). The angle between each pixel and each endmember is calculated – smaller angles represent closer matches – and pixels are assigned to their nearest endmember class. We assigned a threshold of 0.07 rad as the maximum allowable angle between any pixel and endmember; if the calculated angle exceeded this value the pixel was not assigned to any endmember class. SAM is a useful supervised technique for spectral matching as it is largely unaffected by changes in albedo and instead is sensitive to changes in spectral shape. However, if reference library endmembers are not well separated in parameter space (if there are multiple, similar endmembers) SAM can have difficulty assigning a spectrum to the correct endmember class. This is particularly an issue when spectral resolution is low, as angular separation between endmember classes is not well defined.

2.2.2. Infrared Spectrometer for ExoMars (ISEM) and ISEM-E

Mounted below PanCam on *Rosalind Franklin's* optical bench is the Infrared Spectrometer for ExoMars (ISEM) (Korablev et al., 2017). This instrument provides point spectra for a 1° FOV within the larger PanCam FOV and the 4.88° FOV of PanCam's High Resolution Camera (HRC). ISEM uses an acousto-optic tunable filter (AOTF) to cover the wavelengths 1150–3300 nm at variable resolution. Targeting of ISEM will be driven by the discovery of mineralogical and morphological features of interest in PanCam images. ISEM data will enable ground-truthing of CRISM orbital observations free from the influence of Mars CO_2 atmosphere and examine the suite of signatures that contribute to the overall spectral response within a single CRISM pixel. For the ISEM emulator, ISEM-E, we use a handheld field spectrometer (Spectral Evolution RS-3500) with a spectral range of 350–2500 nm and variable spectral resolution (350–1000 nm = 3 nm; ~1500 nm = 8 nm; ~2100 nm = 6 nm). While ISEM will not share any overlapping spectral bands with PanCam, the overlap of ISEM-E and AUPE3 between 438 and 1000 nm allows for

verification of AUPE3 spectra extracted from ROI in multispectral images. The reduced long wavelength limit of ISEM-E (2500 nm) compared to ISEM (3300 nm) does not negatively impact ISEM-E's ability to observe mineralogical variability. Korablev et al. (2017) suggests that ISEM's 3000 nm region is not well suited for mineralogical determination as mineral spectra frequently display a broad, deep absorption in this region due to water in various forms (e.g. adsorbed, fluid inclusions); however, this feature has also been observed in typically anhydrous minerals (e.g. pyroxene). Shorter wavelengths (1400–2500 nm) are well suited to the detection and identification of clays, sulfates, halides, silicates and other hydrated minerals (e.g. Viviano-Beck et al. (2014); Korablev et al. (2017); Bishop (2018)) which we capture within the range of ISEM-E.

ISEM-E was deployed in handheld/contact mode to avoid interference by atmospheric water and to ensure a good signal-to-noise ratio. In handheld mode, ISEM-E was held against the soil surface, which was illuminated with its internal light source, to collect and average 30 individual spectra. ISEM-E collected a single, averaged point spectrum every 40 cm along the NW-SE transect. Once each contact measurement was complete, the surface material was collected for contextual bulk X-Ray Fluorescence (XRF) and Raman analysis. When in contact with surface material the ISEM-E FOV is ~1 cm.

ISEM-E spectra were manually examined for the presence and position of identifiable absorption features. The shifting absorption feature at around 2200 nm in particular was analyzed to determine if Al-OH and Si-OH phases could be discriminated in targets across the transect. As with AUPE3 spectra, PCA was performed on ISEM-E spectra normalized to unit length. To investigate the composition of each ISEM-E target spectrum, spectral fitting was performed on transect target spectra using the MCMC fitting routine. Our reference library contained the same endmembers as for AUPE3 processing, but these were truncated to 1150–2500 nm to approximate the wavelength range of the ISEM instrument. We also performed fitting using the full ISEM-E range (350–2500 nm) which we refer to as the "extended wavelength range" in Section 3.2.6. Prior to processing, the continuum was removed from each ISEM-E spectrum using a convex hull fit which connected local spectral maxima. The continuum was then removed using division. We chose to perform this step to focus on the positions and depths of absorption features for mineral identification, rather than compare absolute differences in reflectance across this wavelength range.

2.2.3. CLose-UP Imager (CLUPI) and CLUPI-E

Mounted on the drill of ExoMars 2020 is the CLose-UP Imager (CLUPI) (Josset et al., 2017). CLUPI is a high-resolution, color camera system designed to mimic what a geologist would observe in the field through a hand lens and provides images of minerals within their original context before they are powdered for geochemical analysis. When at a distance of 10 cm from a target, CLUPI provides 7 μm/pixel resolution with a FOV of 1.9 × 1.3 cm. CLUPI uses a Foveon X3 detector which captures all RGB color information at the same spatial location so, unlike detectors which use a Bayer filter, the resulting image data does not require any interpolation. CLUPI color images will closely represent RGB color from PanCam's filter set and will additionally be calibrated using the CLUPI calibration target located near the drill box (Josset et al., 2017). The CLUPI emulator CLUPI-E used for this study is a Sigma SD15 Digital SLR which uses the same detector as the CLUPI instrument. Its lens is a Sigma 100 mm macro lens which provides a representative field of view and magnification range. The CLUPI-E working distance was approximately 1 m from the surface being imaged yielding a resolution of approximately 0.11 mm/pixel. CLUPI-E was used to collect high-resolution context images of each ISEM-E point spectrum location (at a working distance of either 1 m or 10 cm) so that these sampling locations could be used to accurately situate individual ROIs in AUPE3 images.

2.3. Spectral parameter maps

The full suite of spectral parameter maps from Allender et al. (2020) (see Table 1) was created for AUPE3 and aerial data in the 438–1000 nm wavelength range to enable multiscale comparison between these datasets (Fig. 3). False color images for the 1150–2500 nm range were also created for the aerial dataset in order to compare to ISEM-E ground-level results (Fig. 1-DE). Spectral parameter maps enable band depths and shoulders to be visualized, which can indicate broad mineralogical composition, abundance, or grain size fluctuations. These parameters have proven effective for the MER Pancams (Farrand et al., 2006, 2008, 2013, 2014, 2016; Rice et al., 2010, 2013a) and for orbital imagers like CRISM (Pelkey et al., 2007; Viviano-Beck et al., 2014). Note that spectral parameters are not necessarily diagnostic of specific minerals, rather they test for features consistent with absorptions that indicate the presence of some minerals. For example, the S610_671 parameter tests for the presence of the 650 nm hematite shoulder feature, but other ferric oxides also have similar absorptions, such as the 610 nm feature of goethite.

2.4. Sample analysis

2.4.1. X-Ray fluorescence

Samples collected across the NW-SE ISEM-E transect were powdered to grain sizes <1 mm using a ball mill and a mortar and pestle. Samples were dried overnight at 300˚C. LOI values ranged from 6.8 to 12.2 wt%, relating to the release of structurally-bound water and any minor organic matter present. Values are reported in Table A2 of the Supplement, where Fe_2O_3 represents Total Fe within the sample (Fe_{TOTAL}). Fused discs were created by heating each sample to 1050˚C in a Carbolite CWF1200 oven, and major elements were determined by XRF spectroscopy using an energy-dispersive Spectro XEPOS spectrometer at the University of St Andrews.

2.4.2. Raman spectroscopy

Laboratory Raman analysis was used to approximate what will be observed by ExoMars' Raman Laser Spectrometer (RLS) at the micron scale. Raman analysis was performed at Aberystwyth University using a

Table 1

Spectral parameters calculated for AUPE3 within ExoSpec. From Allender et al., 2020.

| Name	Description	Rationale
LWAC		
S438_671	[(R671-R438)/(671–438)]	Related to degree of oxidation
BD532	[1-(R532/((0.53*R500) + (0.47*R568)))]	Identifies ferric minerals, particularly hematite, and is related to degree of oxidation
BD610	[1-(R610/((0.6*R568) + (0.4*R671)))]	Can indicate goethite development and can be influenced by olivine and pyroxene
S532_610	[(R610-R532)/(610–532)]	Ferric minerals and dust
R671_438	[R671/R438]	Ferric minerals and dust
S610_671	[(R671-R610)/(671–610)]	Indicates hematite absorption by testing for shoulder
RWAC		
R740_1000	[(R740/R1000)]	Ferrous minerals
S740_1000	[(R1000-R740)/ (1000–740)]	Strength and position of NIR absorption linked to ferrous minerals
BD775	[1-(R775/((0.5*R740) + (0.545*R850)))]	Nontronite
BD900	[1-(R900/((0.455*R840) + (0.545*R950)))]	Strength of NIR absorption, related to ferric minerals
S900_1000	[(R1000-R900)/ (1000–900)]	Related to detection of hydrous minerals
BD950	[1-(R950/((0.5*R900) + (0.5*R1000)))]	Related to hydrous minerals, some clays, and silicates
S950_1000	[(R1000-R950)/ (1000–950)]	Linked to detection of hydrous minerals
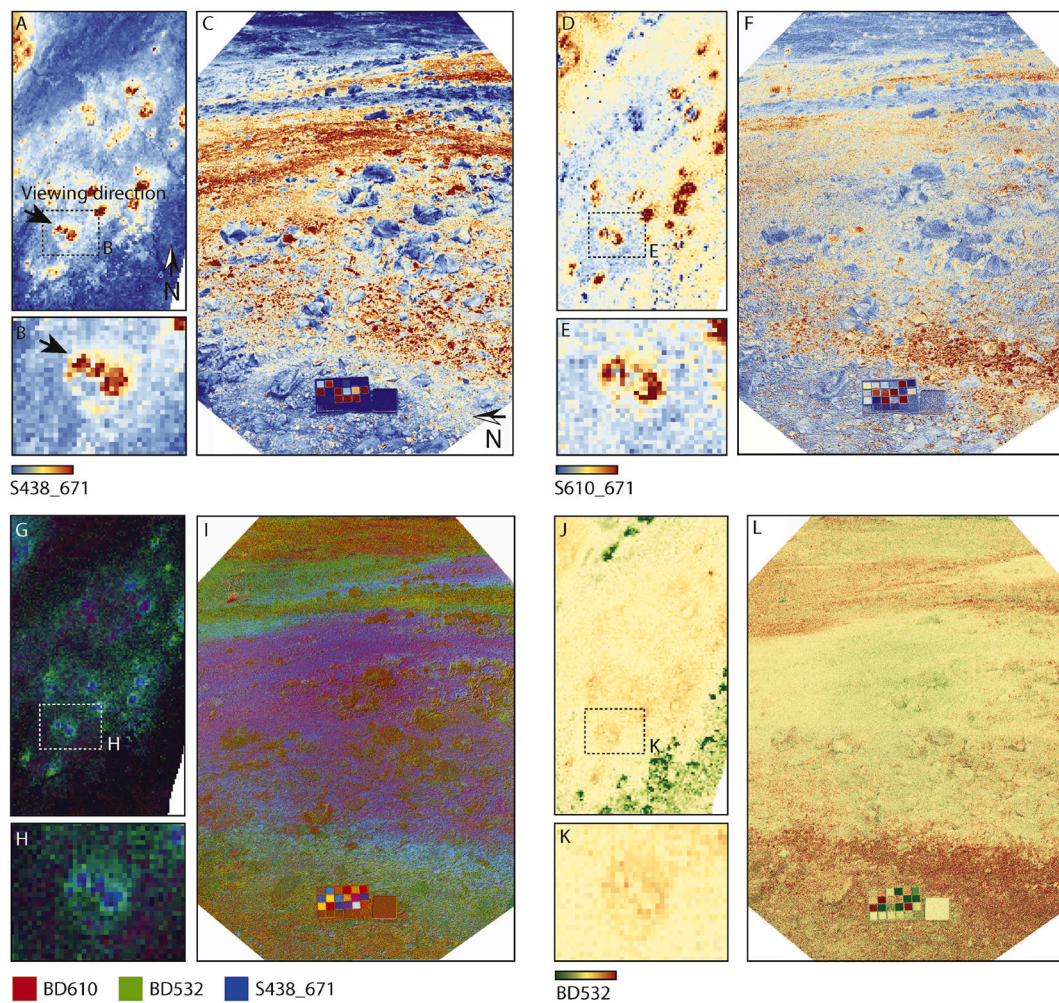
Fig. 3. A: Spectral parameter map S438_671 (blue/red slope) created from Eagle aerial data where red pixels represent higher slope values. B: Inset of the fumarole trio (2 m/pixel) from A. The trio has a higher blue-red slope than the darker basaltic background surrounding the fumaroles. C: AUPE3 image taken facing east (along the direction of the arrow in B). D: Spectral parameter map S610_671 created from Eagle aerial data. Blue pixels may represent goethite-like material, while red pixels may indicate hematite-like material. E: Inset image of fumarole trio from D. F: AUPE3 image taken facing east (along the same direction as the arrow in B). G: Eagle false color image where each color channel is represented by a spectral parameter map measuring Fe-oxidation parameters - see image key. H: Inset image from G. I: AUPE3 image constructed from the same spectral parameter combination used for Eagle in G and H. J: Eagle spectral parameter map of BD532 measuring the depth of the absorption feature at 532 nm indicative of Fe^{3+}-bearing hematite, jarosite, and nanophase oxides (Viviano-Beck et al., 2014). K: Inset of the fumarole trio in J. L: AUPE3 BD532 spectral parameter map. Regions with a large absorption feature at 532 nm appear yellow to red. All scale bars (shown below panels B, E, and K) are 20 m. The MacBeth ColorChecker is approx. 20 cm across. (For interpretation of the references to color in this figure legend, the reader is referred to the web version of this article.)

Horiba Jobin Yvon LabRam HR with a 1200 line/mm grating and a HeNe laser (632.8 nm) coupled with an Olympus BXFM microscope. $20\times$ magnification was used to examine a FOV of 0.24×0.18 mm. The resulting Raman patterns were compared to the RRUFF database (Lafuente et al., 2015) using their CrystalSleuth software to identify potential mineral matches. Several of the target samples exhibited strong fluorescence (typically red soils with a high Fe content) obscuring any Raman bands present – these have been omitted from the results.

3. Results

3.1. Aerial vs ground-based observations

Mean aerial, AUPE3, and ISEM-E spectra averaged from data collected across the entire fumarole trio are shown in Fig. 2. Comparison of these mean spectra show good agreement between AUPE3 and ISEM-E across their overlapping spectral range. The aerial fumarole spectrum likewise shows good agreement of shape across its shared spectral range with AUPE3 and ISEM-E, but no absorption features are observed >1900

nm. Mean AUPE3, ISEM-E and aerial fumarole spectra all possess a steep blue-red 438–671 nm slope (Table 1), but ISEM-E displays 520, 650, and 880 nm VNIR absorption features consistent with hematite. These absorptions are also observed at a coarser spectral resolution in the AUPE3 mean spectrum, but are not visible in the aerial data. In the ISEM-E mean spectrum, the small asymmetric feature at ~1410 nm reveals a higher amount of bound water versus adsorbed water (1460 nm) in the fumarole material (Bishop et al., 2008), which Tarnas et al. (2019) associates with amorphous silica. The broad absorption feature around 2200 nm, with weak features around 2210 and 2260 nm, further indicates opaline silica. In all aerial SWIR spectra, absorption features at around 1400 and 1900 nm are swamped by atmospheric and surface water – as such these regions have been masked. Overall, there is a strong negative trend to the aerial spectra which confirms this high H_2O content as water diminishes the albedo across longer wavelengths.

Comparison of aerial and ground-based spectral parameter maps (Fig. 3) illustrates the level of spectral variability that can be observed at regional and local scales. In Fig. 3-A:C low-albedo, red-brown soils and the surrounding basaltic substrate (Figs. 1-CG and 4-A) have low
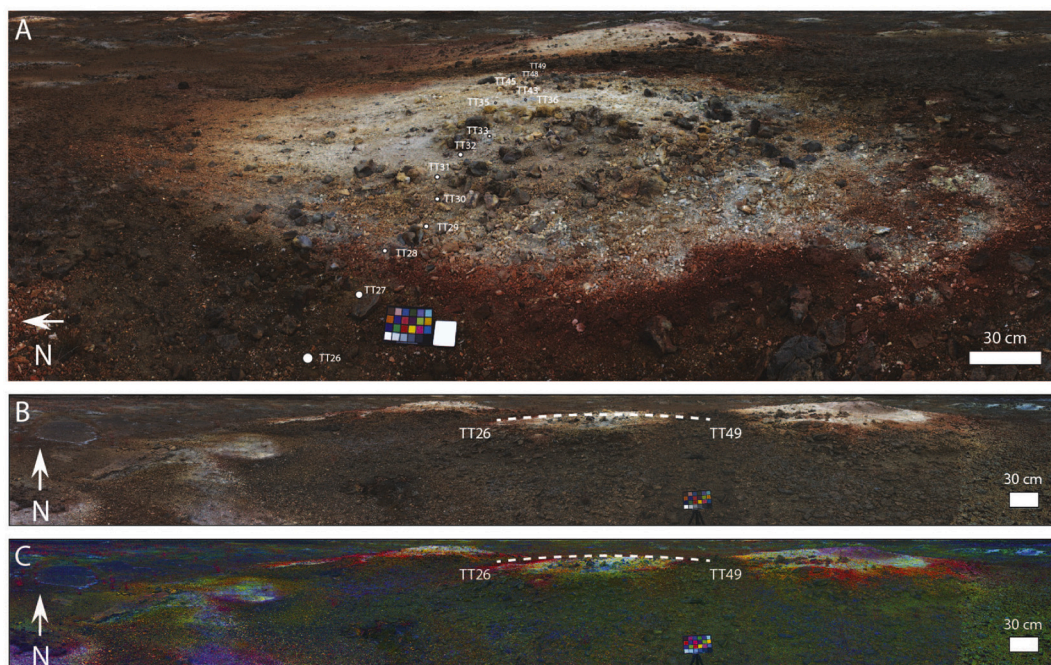
Fig. 4. Panel A shows an AUPE3 image mosaic taken from the edge of the center fumarole facing east. The NW-SE transect (from which AUPE3 spectra, ISEM-E spectra, and XRF samples were taken) is overlain on this image for reference (greater detail is shown in Fig. 5-B, and individual target spectra are visible in Fig. 6-A). True color differences between materials that display different spectral characteristics in Fig. 3-CFIL are highlighted. To provide wider regional context Panel B shows a view of the NW-SE transect spanning all three fumaroles taken facing north. The decorrelation stretch in Panel C shows the same spectral transition pattern is common to all three fumaroles.

reflectance values in both blue and red spectral regions – this subsequently causes the slope value measured by S438_671 to be low (blue pixels). The float rocks in the fumarole center of Fig. 3-C share these S438_671 properties, which are captured in AUPE3 spectra but not aerial spectra. These ground-level features are distinguished from the lighter-toned alteration soils and rock surface coatings found across the fumarole center in the RGB. The regional pattern of these altered soil patches can be observed in the aerial view (Fig. 3-AB) highlighting the majority of inactive fumaroles across the Hverir geothermal field.

Preliminary differentiation of ferric oxide minerals can be observed using the S610_671 spectral parameter which measures the presence and strength of a shoulder at 610–650 nm (Table 1). We tested the S610_671 parameter with multiple samples of goethite and hematite from the RELAB spectral database and found that S610_671 values which are either negative or very slightly positive infer the presence of goethite, and positive S610_671 values infer the presence of hematite. Consistent with the mineralogy derived by Carson (2015), in Fig. 3-D:F we observe "goethite-like" material (blue pixels) at the edges of, and surrounding the fumaroles; while hematite-like material is present throughout the region and within fumarole aprons. The transformation of goethite to red hematite typically occurs with increased temperatures consistent with the conditions approaching the fumarole center (Das et al., 2011; Dehouck et al., 2017). The reddened fumarole apron outlines are clearly visible in the foreground and background of Fig. 3-F.

Three-band combinations of spectral parameters can also be used to measure variability at a site. Primary colors in Fig. 3-G:I represent pixels with spectral features (band depths or slopes) in one of the three spectral parameter maps BD610, BD532, and S438_671 (Table 1). The intensity of color corresponds to the strength of the feature. For example, red pixels in Fig. 3-G:I possess a band depth at 610 nm which is indicative of goethite, which agrees with results in Fig. 3-F. Green pixels represent spectra with an absorption feature at around 532 nm related to Fe^{3+}-bearing jarosite, nanophase oxides, and hematite. Secondary colors in Fig. 3-G:I indicate pixels whose spectra possess absorption features in multiple spectral parameters. For example, magenta pixels represent

spectral signatures with a 610 nm absorption feature and a positive slope across 438 to 671 nm. These correspond to light-toned, pink/peach sediments in Fig. 4-A). At the 2 m/pixel aerial scale in Fig. 3-H, the magenta pixels in the fumarole halo centers are not resolved, however, they are detectable for fumaroles in northern Hverir, there may be larger alteration patterns, or more heavily hydrothermally altered terrain in that region. Cyan pixels represent spectra with an absorption feature at ~532 nm which can indicate Fe^{3+}-bearing hematite, jarosite, or nanophase oxides and a steep positive slope across 438 to 671 nm. These cyan regions correspond with hematite-bearing regions in Fig. 3-F and bright red sediments in Fig. 4-A.

In Fig. 3-L strong BD532 features (red pixels) correspond to the reddened soils at the edge of the fumarole apron. Weaker spectral signatures, which we interpret to correspond to lesser hematite abundances, are distributed across the majority of the fumarole apron as light-toned pink soils (yellow pixels). From Fig. 3-K hematite enrichment does not occur in the fumarole centers, but within and surrounding the aprons, in agreement with the results in Fig. 3-F and I.

3.2. Multi-scale analysis of fumarole transect

The true color and decorrelation stretched images in Fig. 4-BC show that a similar alteration pattern is observed across all three fumaroles. For the remainder of this work we focus our investigations and figures on the center fumarole only.

3.2.1. Verifying AUPE3 spectra with ISEM-E

The results of comparing AUPE3 spectra with visible-NIR spectra acquired in the extended wavelength range of ISEM-E are shown in Fig. 5. The 12-point spectrum extracted from target ROIs using AUPE3 data does not always capture the extent of the variation from 500 to 610 nm (e.g. TT28, TT30, TT36, TT49); LWAC spectra are much flatter than their ISEM-E counterparts. However, this is not the case with all target spectra, the majority match well in spectral shape across all filters. ISEM-E spectra possess a more defined 900 nm absorption feature than
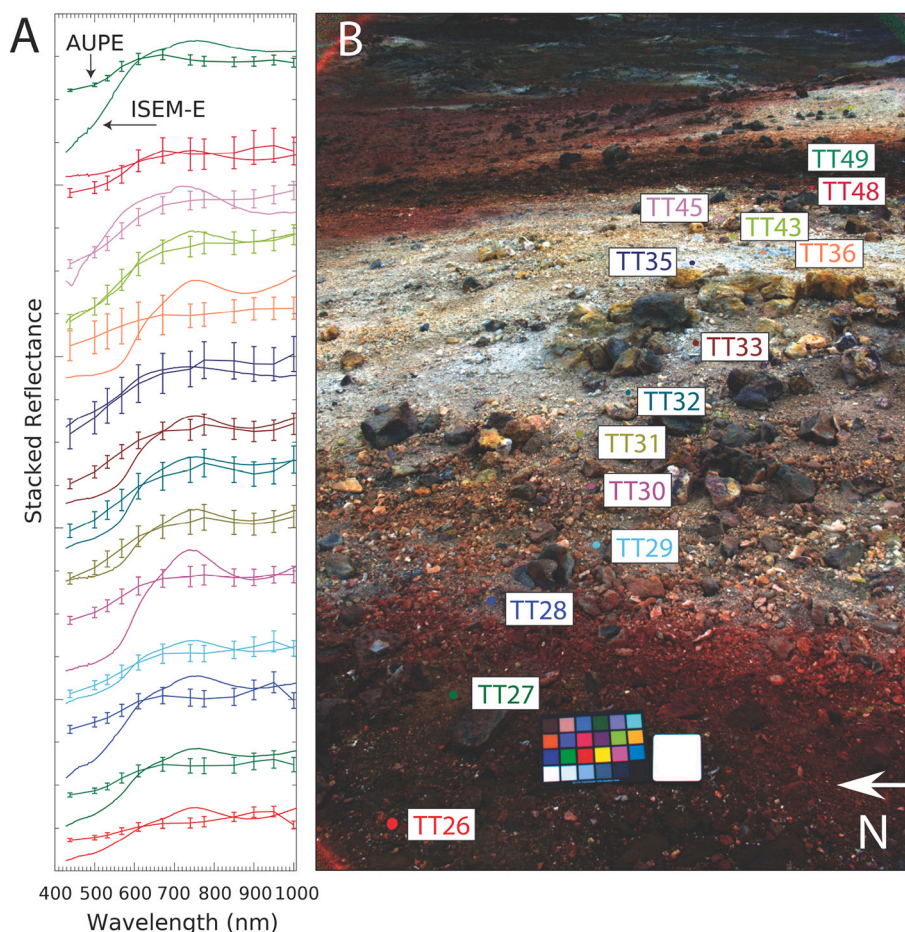
Fig. 5. AUPE3 vs VNIR spectrum from the ISEM-E extended wavelength range. Colors in A correspond to target locations across the center fumarole in B. AUPE3 spectra are displayed with error bars representative of the variance within an ROI for each geology filter.

observed in AUPE3 spectra. This 900 nm feature (along with a 530 nm absorption) is useful for discriminating Fe^{3+} bearing minerals such as hematite, jarosite, and nanophase oxides. AUPE3 spectra in TT30, TT36, and TT49 in particular do not record the 530 nm slope. AUPE3 spectra for TT26, TT27, TT28, TT29, TT48, and TT49 all possess a downturn in reflectance from 950 to 1000 nm. This downturn can be an indicator of hydration state as it can be used to infer the presence of the H_2O combination band or the 3_vOH overtone feature at around 1000 nm in some (but not all) hydrated minerals (Rice et al., 2010, 2013a, 2013b), however, in this case we believe this downturn is an artifact, due to the lack of a similar feature in ISEM-E spectra. This and other discrepancies will be discussed in Section 4.2.

3.2.2. Manual interpretation of AUPE3 spectra

All AUPE3 spectra possess positive 438–671 nm slopes suggestive of oxidized Fe-bearing phases (Fig. 6-A). Targets at the outer edges of the fumarole apron (TT26, TT27, TT28, and TT49) are brown soil mixtures with lower reflectance than any other in-scene material (see Fig. 5-B for soil colors). Targets TT28, TT29, and TT48 have a broad absorption centered near 820 nm, which can be an indicator of hematite crystallinity, although other features consistent with hematite (absorptions around 520, 650, and 880 nm) are not readily apparent from their AUPE3 spectra particularly since the 650 nm shoulder lies between two AUPE3 filters. However, we are able to estimate the presence of this shoulder in AUPE3 spectra using the spectral parameter S610_671 (Fig. 3-D:F).

The light-toned pink soils (TT30, TT31), purple/white soils (TT32) and pink/white soils (TT33) toward the fumarole center (Fig. 5) display

an absorption feature centered around 900 nm which represents an Fe^{3+} field transition that can relate to hematite, jarosite, and nanophase oxides. In the ISEM-E spectra in Fig. 5-A a shoulder at 650 nm is visible along with an absorption feature at 520 nm, indicating hematite is responsible for the pink/purple color of these light-toned soils, visualized in Fig. 3-D:F. Target TT35 is a pink/white soil sample whose 900 nm absorption feature appears shifted to between 900 and 950 nm which may instead indicate the presence of goethite rather than hematite. Target TT36 is spectrally flat across all AUPE3 wavelengths yet its ISEM-E spectrum (Fig. 5-A) shows a strong hematite signature. From AUPE3 spectra it is apparent that TT45 is a pink/grey soil, however it is spectrally flat from 740 to 1000 nm while its ISEM-E spectrum suggests that it possesses an absorption feature at a longer wavelength (e.g. centered at 1000 nm) which is suggestive of the Fe^{2+} transition common to olivine or pyroxene. The brown soil sample TT49 also shares this 1000 nm centered feature. The AUPE3 spectrum of orange/brown soil (TT48) possesses an Fe^{3+} crystal-field absorption feature between 780 and 860 nm which could be an indicator of hematite (Bell et al., 2000; Lane et al., 1999) – this differs from its ISEM-E spectra in Fig. 5-A, which instead shows a shallow feature around 900–950 nm that could indicate goethite, which is supported by its orange appearance in the RGB AUPE3 image.

3.2.3. Visualization of spectral variability

Fig. 7 shows PCA results for both AUPE3 and ISEM-E target spectra. Data points at the farthest extents of this graph (with the largest or smallest PC values) represent the most spectrally unique signatures. For both AUPE3 and ISEM-E the first two principal components capture over
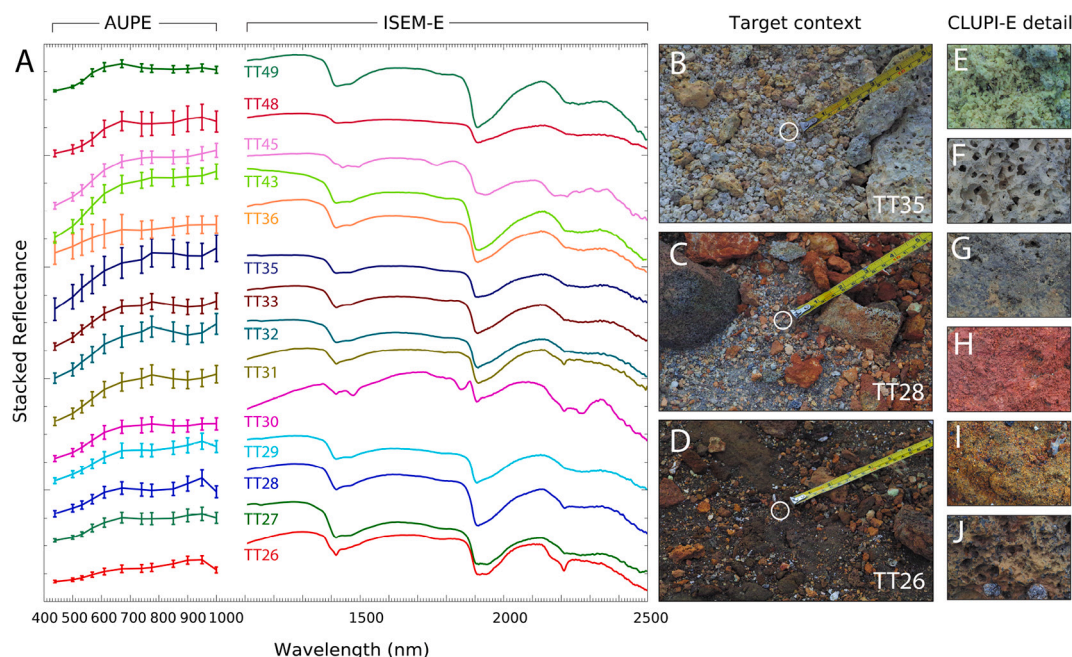
Fig. 6. Colors in A correspond to target locations across the center fumarole in Fig. 5-B. All CLUPI-E detail images (*E-J*) are 26.4 mm in width. A: Average AUPE3 spectra extracted from each ROI are displayed alongside their corresponding ISEM-E (1150–2500 nm) spectrum. B: Context image showing the location of the 1 cm ISEM-E FOV for TT35. The FOV contains material from CLUPI-E detail images F, G, and I. C: Context image showing location of TT28 1 cm FOV. The FOV contains material from CLUPI-E detail images I, F, and G. D: Context image showing location of TT26 1 cm FOV. This FOV contains material from images I and J. E-J: To illustrate changes in color and texture of solid rock across the fumarole apron CLUPI-E detail images are displayed. For these the CLUPI-E working distance was 10 cm from the sample (0.01 mm/pixel), thus the width of each CLUPI-E image is 26.4 mm.

80% of the variance in the data.

The most spectrally unique AUPE3 targets at the edges of the data cloud are TT26, TT27, TT36, TT48, and TT49. These targets are highlighted whether using the full set of 12 geological filters (Fig. 7-A) or a reduced set of only the LWAC RGB filters (Fig. 7-B). Figs. 7-D and 5-B show these targets are type examples representative of each fumarole zone: the red-brown surroundings, yellow-soils, grey-soils, and red-soils respectively. For AUPE3, PC 1 shows the progression from more oxidized alteration phases at the fumarole edges to phases typical of aggressive chemical leaching at the fumarole center. By contrast, PC 1 for ISEM-E spectra captures information from the hydration feature at ~1900 nm to record the diversity within the fumarole alteration halo (Fig. 7-C), highlighting TT26, TT27 and TT36 as outliers and including TT30, TT31, and TT45 which have features of interest within the SWIR (Fig. 6-A). AUPE3 data effectively captures the intra-scene mineralogical variability despite having fewer absorption bands present within the VNIR (438–1000 nm) wavelength range.

The result of SAM classification of AUPE3 imagery using scene-selected endmembers is displayed in Fig. 8. Red soils spatially agree with regions shown to contain Fe^{3+} such as hematite in Fig. 3-F&L, light soils are consistent with leached, silica-rich targets visualized in Fig. 9-D, and yellowed soils show the positions of yellowed pebbles and float rock coatings within the scene. Note that since this SAM classification was only performed on LWAC spectra, which span 438–671 nm, the result is not able to capture spectral diversity from longer wavelength AUPE3 NIR bands, or from hydrated mineral features that are only present in the SWIR.

3.2.4. Investigation of key absorption features

Fig. 9-A shows the variation in hydration state across transect targets. The majority of targets have 1900 nm absorption features that are approximately twice as deep as their 1400 nm feature – this is common in hydrated minerals due to OH and H_2O overtone bands in these regions and has resulted in these targets being distributed along a positive trend line. At the lower boundary of the trend line (e.g. targets TT30 and

TT45) these absorptions are much weaker, consistent with sulfates such as jarosite. Targets TT27, TT29, and TT36 possess the deepest OH and H_2O features. These samples are located in different zones of the fumarole apron, and have different RGB color characteristics, yet they share very similar ISEM-E spectral features in the SWIR (Fig. 6-A). In Fig. 9-B, targets TT30 and TT45 are located away from the trend line. They possess multiple absorptions around 2210 nm (shown in Fig. 9-F), but have weaker 1910 nm features with respect to the other targets. These spectral characteristics are consistent with Al-OH and kaolin group minerals. Targets following the trend line in Fig. 9-B possess a single, broad 2210 nm feature (Fig. 9-F) consistent with hydrated silica (Fig. 6-B). Targets in Fig. 9-C that follow the trend line possess features of similar depth at 2210 and 2260 nm, consistent with a broad shallow hydrated silica absorption across these wavelengths (Viviano-Beck et al., 2014). We again see TT45 deviate from the trend line, suggesting a different composition – Fig. 9-F shows it possesses three weak absorptions across this range. In Fig. 9-C, TT30 now lies on the trend line, however, unlike the other targets it possesses two distinct absorptions (Fig. 9-F) rather than a single broad feature consistent with hydrated silica. All plots in Fig. 9 demonstrate the difficulty in obtaining distinct mineralogical classifications for these samples in the SWIR as target sediments are intimately mixed and likely composed of poorly crystalline phases that don't possess sharp absorptions across the ~2200 nm range.

Fig. 9-D shows that when using AUPE3 data the Fe^{3+} band depths at ~500 and ~900 nm are able to separate the targets into two groups corresponding to their locations at the edges (Fe-rich) or center (Si-rich) of the alteration apron. The ISEM-E data in Fig. 9-E shows the relationship between Fe^{3+} band depths at ~500 and ~900 nm using ISEM-E. Targets within the dashed box, which delineates approximately equal band depths, predominantly correspond to the Fe-rich red/brown soils at the edges of the fumarole apron. Moving toward the center of the fumarole, samples which represent high-albedo pink/grey to white soils (e.g. TT31, TT33, TT36) instead exhibit much deeper features at around 500 nm, combined with a shallow 900 nm feature. Exceptions to this are
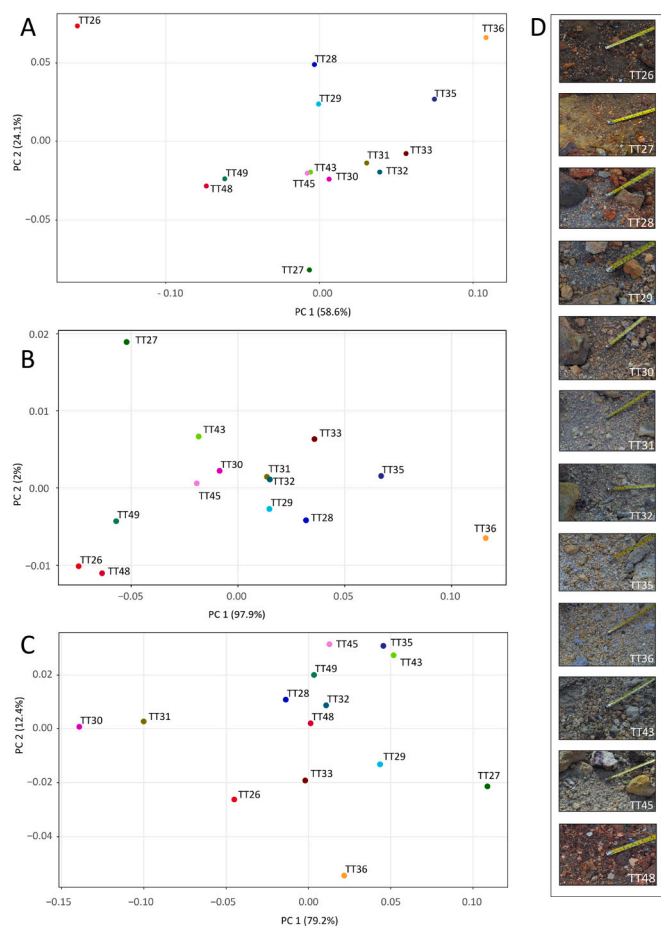
Fig. 7. A: PCA results for AUPE3 spectra calculated using the set of 12 geological filters. B: PCA results for AUPE3 spectra calculated using a subset of 3 LWAC RGB filters, which still capture intra-scene diversity. C: PCA results for ISEM-E spectra calculated using the 12 geological filters. D: Context images showing target diversity across the transect.

TT35 and TT43, which are both pink/white targets located within the fumarole center which have very small, symmetrical absorptions at both of these wavelengths. Discrepancies between these two datasets are discussed in Section 4.2.

We investigated whether the broad 2200 nm absorption feature common to most targets can be used to discriminate between Al-OH materials, hydrated silica, and sulfates, and whether it shifts with alteration zone across the fumarole apron. The ~2200 nm OH-combination band consistent with Al-OH materials (e.g. clays) can shift to longer wavelengths (approx. 2280–2320 nm) as Al is exchanged for Mg or Fe at the octahedral sites in the mineral structure (Bishop et al., 2008; Bishop, 2018). Hydrated silica exhibits an absorption band at around 2210–2220 nm due to Si-OH combination tones and a 2260 nm band due to H-bound Si-OH (Viviano-Beck et al., 2014). The potassium-iron sulfate mineral jarosite also exhibits absorption features at around 2212 and 2265 nm, while a doublet feature centered at 2160 nm and 2210 nm is indicative of the aluminosilicate kaolinite. Fig. 9-F shows the positions of these band minima across the transect. For TT29, TT35, TT36, TT43, TT45, TT48, and TT49 the 2200 nm feature shifts to slightly longer wavelengths (2250 nm for TT29, and ~2215–2220 nm for all others). Weaker, secondary minima are observed for TT30 and TT45; TT30 possesses the characteristic absorption features of jarosite (Figs. 6-A and 9-F) which can be formed through the oxidation of iron sulfides in acidic environments (Herbert, 1997) or from basaltic precursor minerals with the addition of sulfur (Farrand et al., 2009; Hynek et al., 2013) as at Námafjall.

As the majority of targets have absorption features at 1400, 1900, and 2210 nm they could be interpreted as Al-OH clays, however, most targets display a broad feature rather than the sharp absorptions usually consistent with crystalline Al-smectites indicating they contain either poorly crystalline Al-OH phases, amorphous Si-OH material (Tarnas et al., 2019) or some mixture of both. Our analysis of target absorption positions shows that these Al-OH and Si-OH phases cannot solely be discriminated using ISEM-E. While it is possible for Al-OH phases to be produced as hydrothermal alteration products, it is likely given the increasingly acidic alteration environment toward the fumarole center that targets predominantly contain Si-OH phases.

We use a parameter space from Sun and Milliken (2018) to estimate the crystallinity of aluminosilicate phases within target sediments
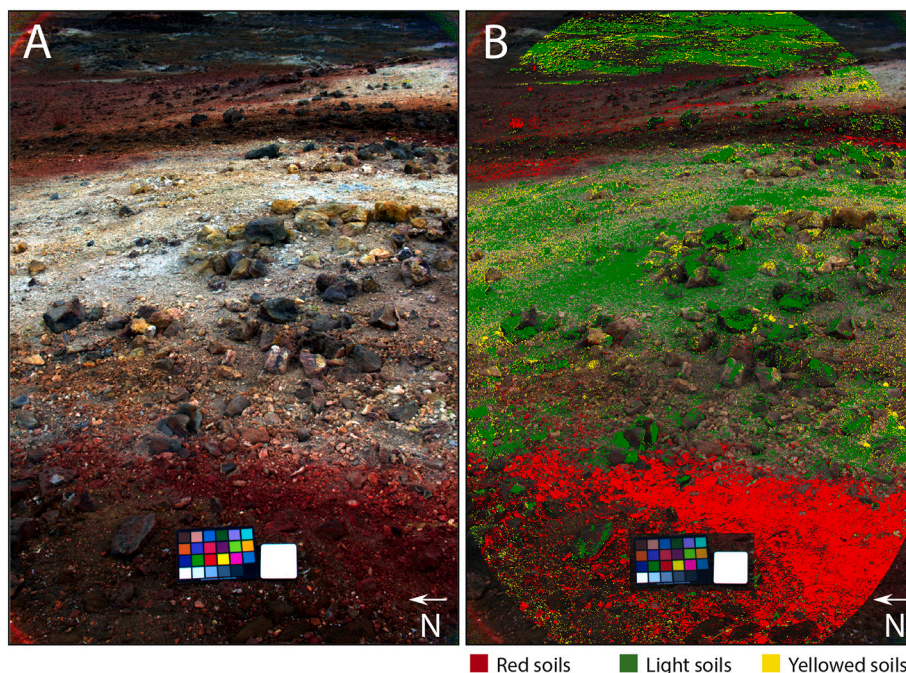

Fig. 8. A: RGB context image of the AUPE3 scene. B: SAM classification result using endmembers selected from an MNF image as an endmember library. Yellow pixels correspond to "yellowed soil", green pixels to "light-soils", and red pixels to "red soils". The "shade" and "unclassified" endmembers has not been displayed for clarity. Unclassified pixels are those that have not been assigned a class as the spectral angle between endmember spectra exceeded the spectral angle threshold of 0.07 rad. (For interpretation of the references to color in this figure legend, the reader is referred to the web version of this article.)
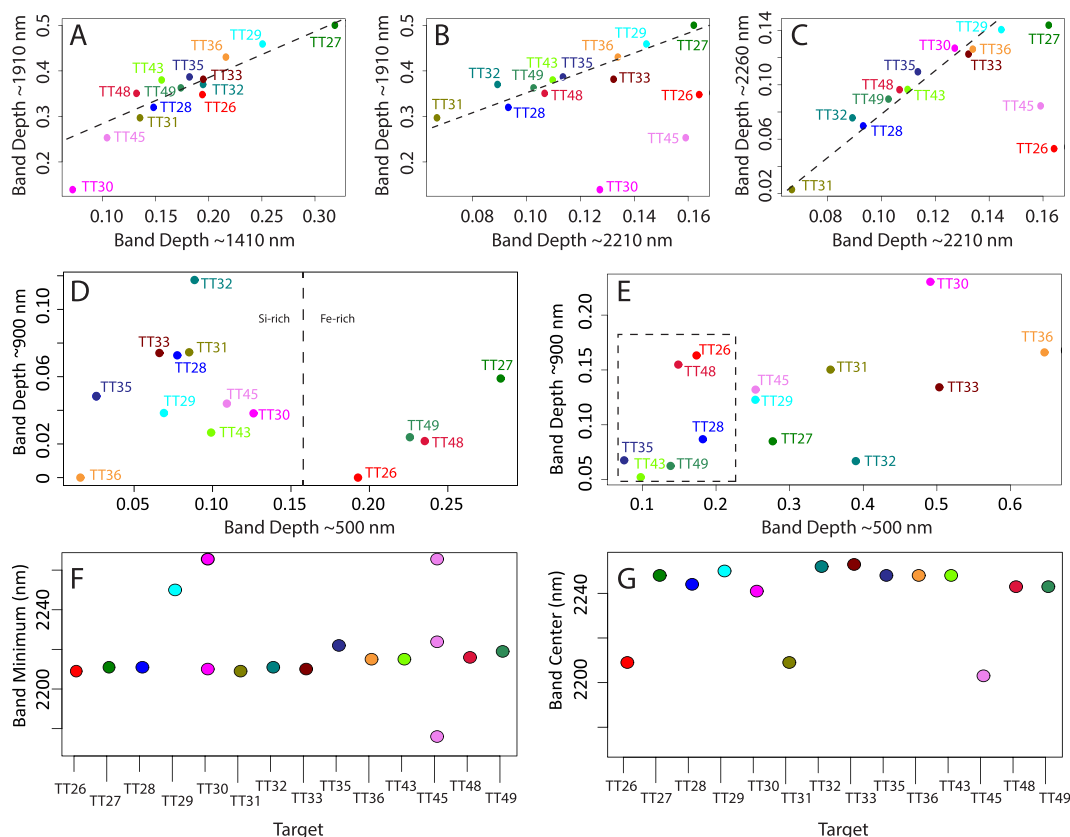
Fig. 9. ISEM-E and AUPE3 band depth analysis across the fumarole transect (A-C): A: 1410 nm OH feature vs the 1910 nm H_2O feature. B: 2210 nm Al-OH/Si-OH feature vs 1900 nm hydration feature. C: Hydrated silica absorption features. Samples which lie on the trend line display strong evidence for hydrated silica. D: AUPE3 Fe^{3+} band depth plot. E: ISEM-E plot showing Fe^{3+} band relationship. Samples within the dashed box have absorption features of a similar depth. F: Plot of absorption band minima at ~2200 nm. A small shift to longer wavelengths is visible for samples greater than and including TT35. G: Plot of the absorption band center at 2200 nm (indicates overall band symmetry). Samples with the same nm values in panels F and G are symmetrical about their minimum.
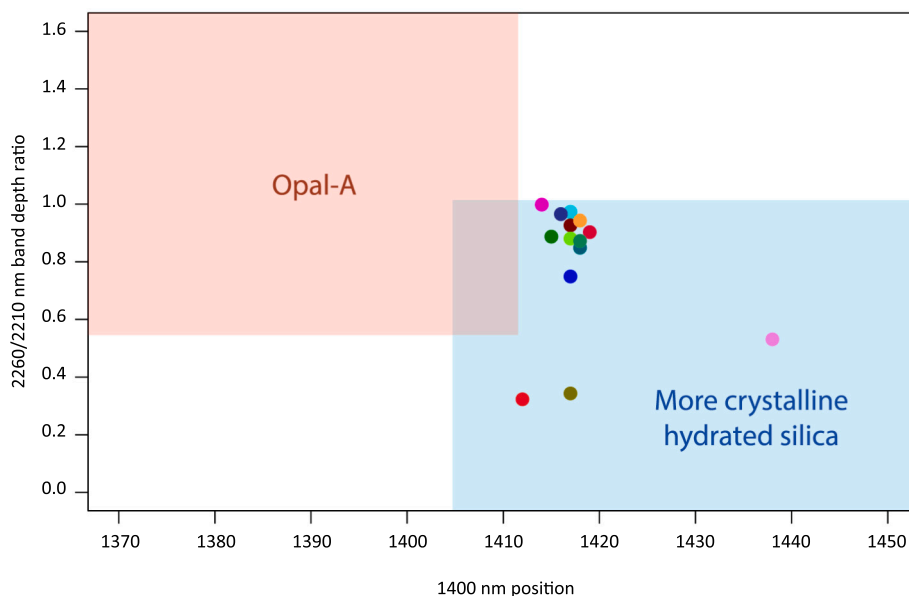

Fig. 10. Plot depicting the parameter spaces for amorphous and crystalline silicate materials as a result of the shifting 1400 nm band depth position vs the 2260/2210 band depth ratio (Sun and Milliken, 2018). Colors correspond to those in Fig. 6.

(Fig. 10). This parameter space was developed for mapping amorphous and crystalline silica, and cannot discriminate whether targets contain poorly crystalline Al-OH or amorphous Si-OH, but can provide a measure of the relative crystallinity of the intermixed target sediment. We find that all targets contain poorly crystalline phases i.e. phases that possesses some crystal structure relative to amorphous material (Opal-

A). Outliers in this plot (TT26, TT31, and TT45) represent targets containing phases with some crystalline structure which possess distinct features around ~2210 nm in agreement with the ISEM-E results in Fig. 9-BC. It is possible that these targets could contain poorly crystalline Al-OH phases as they are located away from the fumarole center.

3.2.5. XRF and Raman results

Brown and red soils found on the apron of the center fumarole are enriched in Fe$_2$O$_3$, Al$_2$O$_3$, CaO, and MgO but exhibit low TiO$_2$ and SiO$_2$ (Fig. 11-A:E). Lighter-toned soils at the fumarole center (see Fig. 4-A) are depleted in all major elements, with the exception of TiO$_2$ and SiO$_2$. Therefore, phases high in Fe, Ca, or Al such as hematite, gypsum, or Al-clays should be located toward the edges of the fumarole apron, while samples high in hydrated silica are located toward the fumarole center.

This facilitates discrimination between the poorly crystalline Al-OH and amorphous Si-OH phases observed in Section 3.2.4 by ISEM-E. Fig. 11-G: J additionally relate the spectral position of the SWIR Al-OH and Si-OH combination bands observed by ISEM-E (2200–2250 nm) to the underlying target chemistry. The chemical leaching of Al and Fe and the relative enrichment of Si is emphasized via the separation of target data points into two distinct alteration regions (Fig. 11-G:I). However, due to the lack of well-defined absorption features in this wavelength region no quantifiable relationship is observed between the position of the Al-OH/Si-OH band minima and underlying chemistry.

When we tested the relationship between the metal-OH combination absorption feature (2280–2320 nm) to FeO and MgO content in crystalline clay minerals for these intermixed, poorly crystalline sediments (Fig. 11-J), unlike Michalski et al. (2015) we did not see a definitive

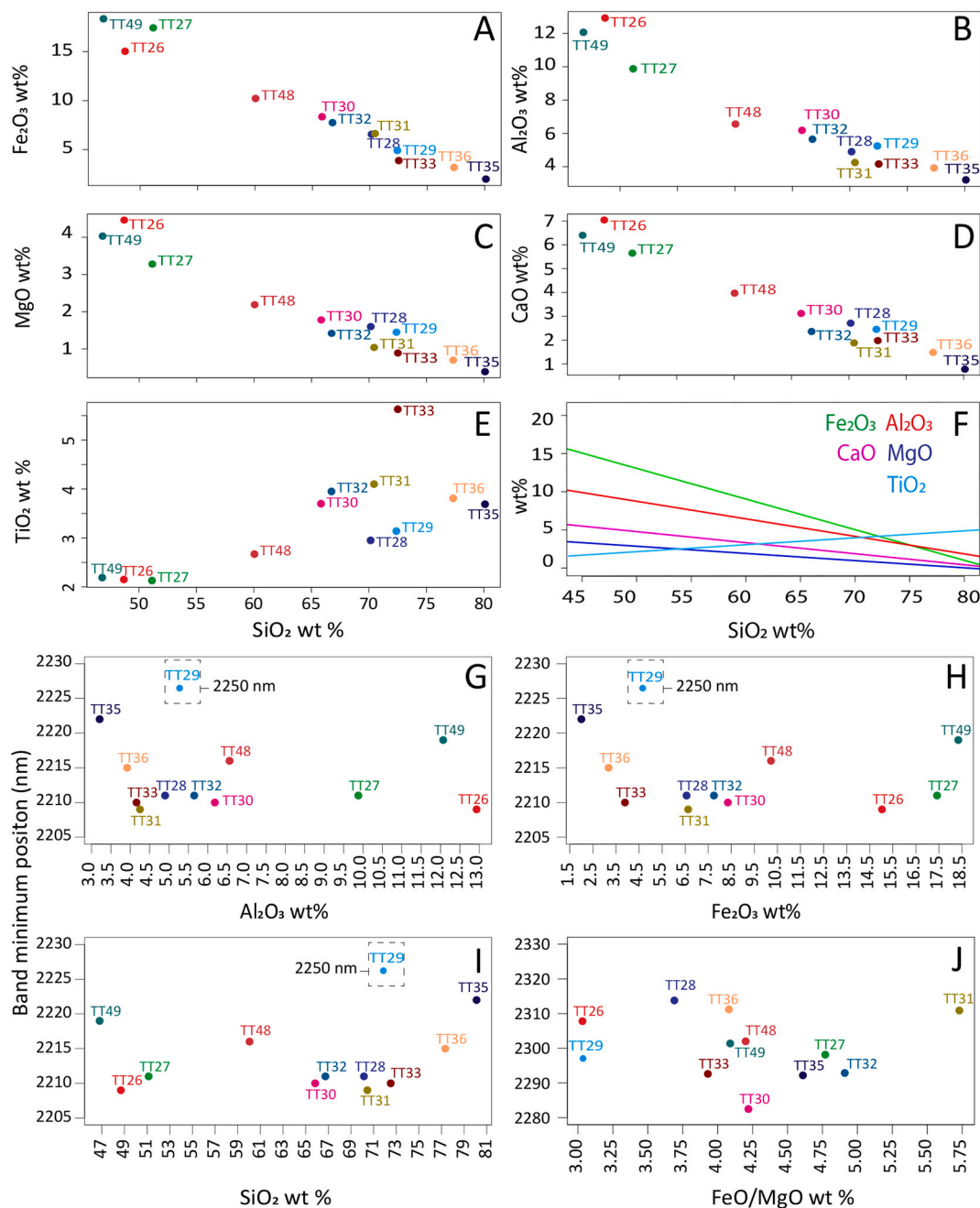**Fig. 11.** XRF scatter plots showing the depletion of Fe$_{TOTAL}$ (A), Al$_2$O$_3$ (B), MgO (C), CaO (D) and enrichment of TiO$_2$ (E) across the fumarole transect from the edge to the center as a function of Si. The gradient for each of these elements is shown in (F). Sample (G) Al$_2$O$_3$ wt%, (H) Fe$_2$O$_3$ wt%, (I) SiO$_2$ wt% and (J) FeO/MgO wt% vs wavelength of Al-OH or Si-OH absorption.

separation of targets into groups with similar spectral and chemical properties because all our targets fall within their low-moderate FeO/MgO classification (2–10 wt%) but band minima for our targets span the entire 2280–2320 nm range. Thus, the fumarolic alteration environment produces clay phases which are difficult to discriminate spectrally and geochemically in mixed Si-rich, poorly crystalline sediments.

Fig. 12 shows the results of laboratory Raman spectroscopic analysis of randomly-selected spot sites within target sediments, and is approximately analogous to what would be observed by ExoMars RLS at the micron scale. Within these highly intermixed sediments, Raman spectroscopy identifies anatase, Ca-heulandite (TT30), and gypsum (TT32 and TT33) (Lafuente et al., 2015). Anatase (TiO$_2$ polymorph) is found in all targets, and is a common reprecipitation product following acid-leaching of basalt (Carson, 2015). It produces strong Raman peaks and is easily detectable in altered volcanic soils but can overwhelm and mask the signal from other materials (Black and Hynek, 2018). Cross-referencing these results with the XRF elemental compositions we
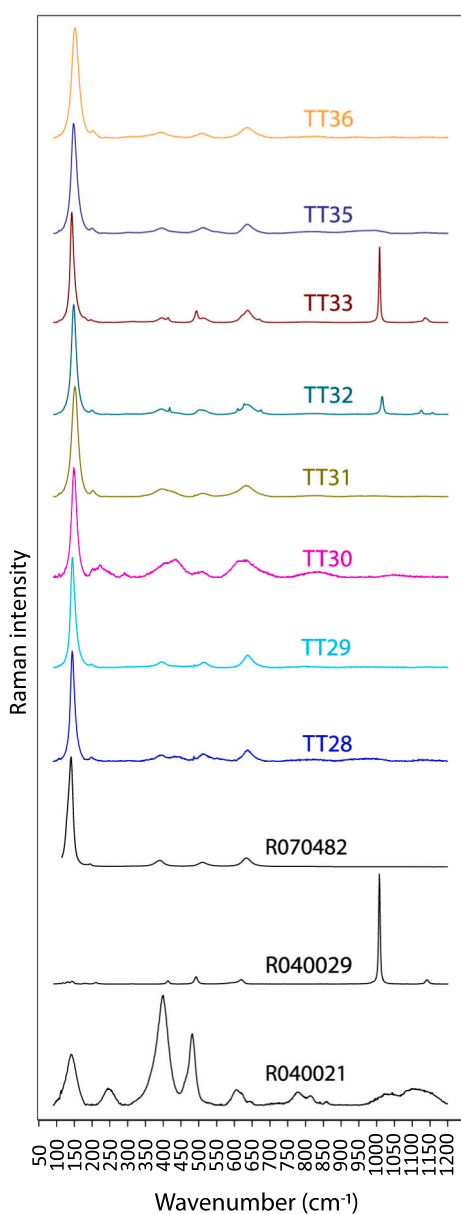
observe high TiO$_2$ in altered soils toward the fumarole center (Fig. 11).

3.2.6. Spectral fitting results

Monte Carlo spectral fitting results for AUPE3 (438–1000 nm), ISEM-E (1150–2500 nm) and the extended wavelength range which spans both these instruments (350–2500 nm) are shown in Fig. 13. The AUPE3 results in Fig. 13-A favor relative contributions from Si-bearing phases in a manner that is consistent with XRF results (Fig. 11), but hisingerite and zeolite endmembers have been preferentially fitted over siliceous sinter (opaline silica). Fe-oxides like hematite and goethite are more strongly favored toward the fumarole edges, which is again consistent with the spectral summary parameters in Fig. 3-BD and XRF results (Fig. 11). MCMC fitting identifies sulfates in the mid-apron of the fumarole which are also seen in the spectral summary parameters (Fig. 3-G:L) and clays (particularly Al-rich illite) are found toward the fumarole center. This distance dependent alteration pattern is not as clear in the ISEM-E fitting results. Opaline silica is preferentially selected by the fitting routine across all targets; clays and sulfates also show no distinct alteration pattern and are identified generally across the fumarole. Fe-oxides were fitted in smaller amounts in all targets, except for TT26 and TT27 (which are the darkest red sediments and those which we would expect to contain Fe-oxides). The gypsum endmember was fitted to all target spectra except TT30 (Fig. 13-B), however, Raman only identifies gypsum in the TT32 and TT33 (Fig. 12). The Ti-oxide anatase has instead been fitted to the TT30 spectrum, which is a component of this target's (and all targets) Raman spectrum. The extended wavelength range shows similar results to those of ISEM-E, except that the inclusion of shorter VNIR wavelengths (440–1000 nm) has meant that contributions from Fe-oxides were estimated to be higher across the fumarole center. Both ISEM-E and extended wavelength ranges show a similar pattern of clay and gypsum contributions, although gypsum has instead been preferentially fitted to several targets where it has replaced clay (e.g. TT36). Anatase was fitted to multiple targets in this wavelength range, which is in agreement with Raman results (Fig. 12). Sulfate contributions are not present in extended wavelength models of central targets, however, TT43, TT45, TT48 and TT49 show very similar sulfate contributions (in green shades) to ISEM-E.

The spectral plots in Fig. 14 show that the Monte Carlo fitting routine produces variable results across the AUPE3, ISEM-E, and extended wavelength ranges. In the first column of Fig. 14 we see that the AUPE3 wavelength range for targets TT29, TT30, and TT45 primarily fits Fe-oxides, Fe-silicates, zeolites, and K—Fe sulfates. For TT29 (Fig. 14-A), we see that the modeled spectrum (red) is not well fit to the target (black) as it doesn't reflect the broad absorption centered at around 825 nm. Extending into the ISEM-E wavelength range (column 2) we see contributions from siliceous sinter (opaline silica) and a variety of Al- and Fe-clays, Fe-sulfates and Fe-oxide phases. However, we also see that some endmembers have again been fitted that don't model the input spectrum well. For example, in TT29 (Fig. 14-B) the target spectrum (black) doesn't possess any absorption around 1800 nm; however, as gypsum has been selected as a contributing endmember the fitted spectrum (red) does possess this feature. The extended wavelength range (column 3) shows that each target records a combination of mineral phases detected at AUPE3 and ISEM-E wavelengths as expected, with the exception of TT30, which records a new contribution from kaolinite. Uncertainties associated with all fits are provided in the Supplementary Information along with the full range of contributing endmembers (not only the top 3).

All results from Section 3.2 above are summarized in Table 2.

4. Discussion

4.1. Aerial vs ground-based SWIR reflectance

PanCam observations will be guided, in-part, by observation of surface features in orbital hyperspectral (i.e. CRISM), and RGB/VNIR
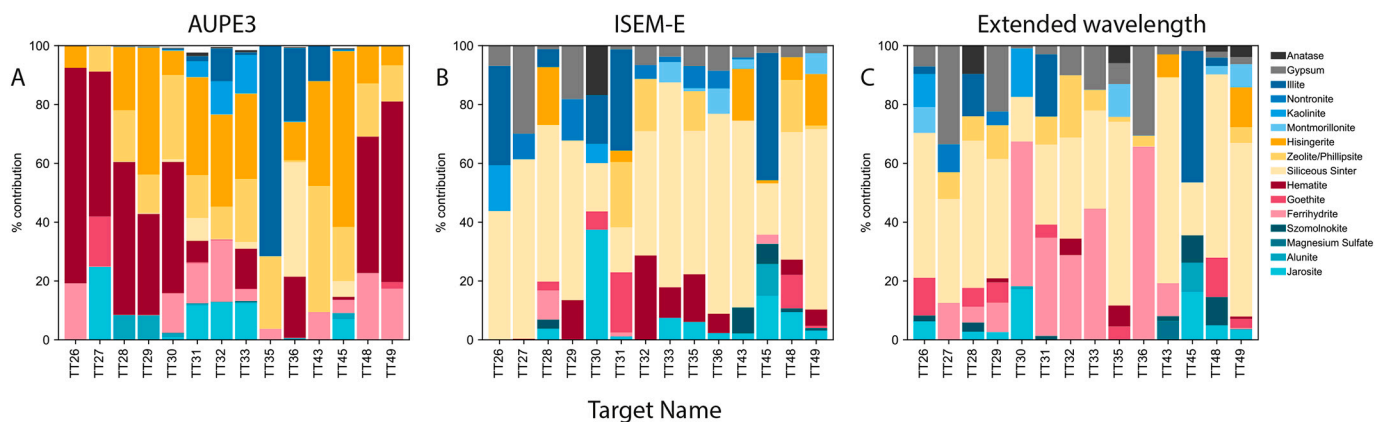

Fig. 12. From bottom to top: RRUFF samples of Ca-heulandite, gypsum, and anatase; followed by transect target samples progressing from the fumarole edge to its center.

Fig. 13. Spectral fitting results for A: AUPE3, B: ISEM-E and C: Extended wavelength range. Each bar represents a target, and colors illustrate the percentage contribution of specific endmembers to that targets spectral signature. Fe-oxides are shown in shades of red, clays in shades of blue, sulfates in shades of green, and silicates in shades of yellow. The TiO polymorph anatase is shown in black, and gypsum (CaCO$_3$) in grey. All wavelength ranges show Si has been fitted across the fumarole transect, however, only AUPE3 records an increase in Si contribution toward the fumarole center. (For interpretation of the references to color in this figure legend, the reader is referred to the web version of this article.)
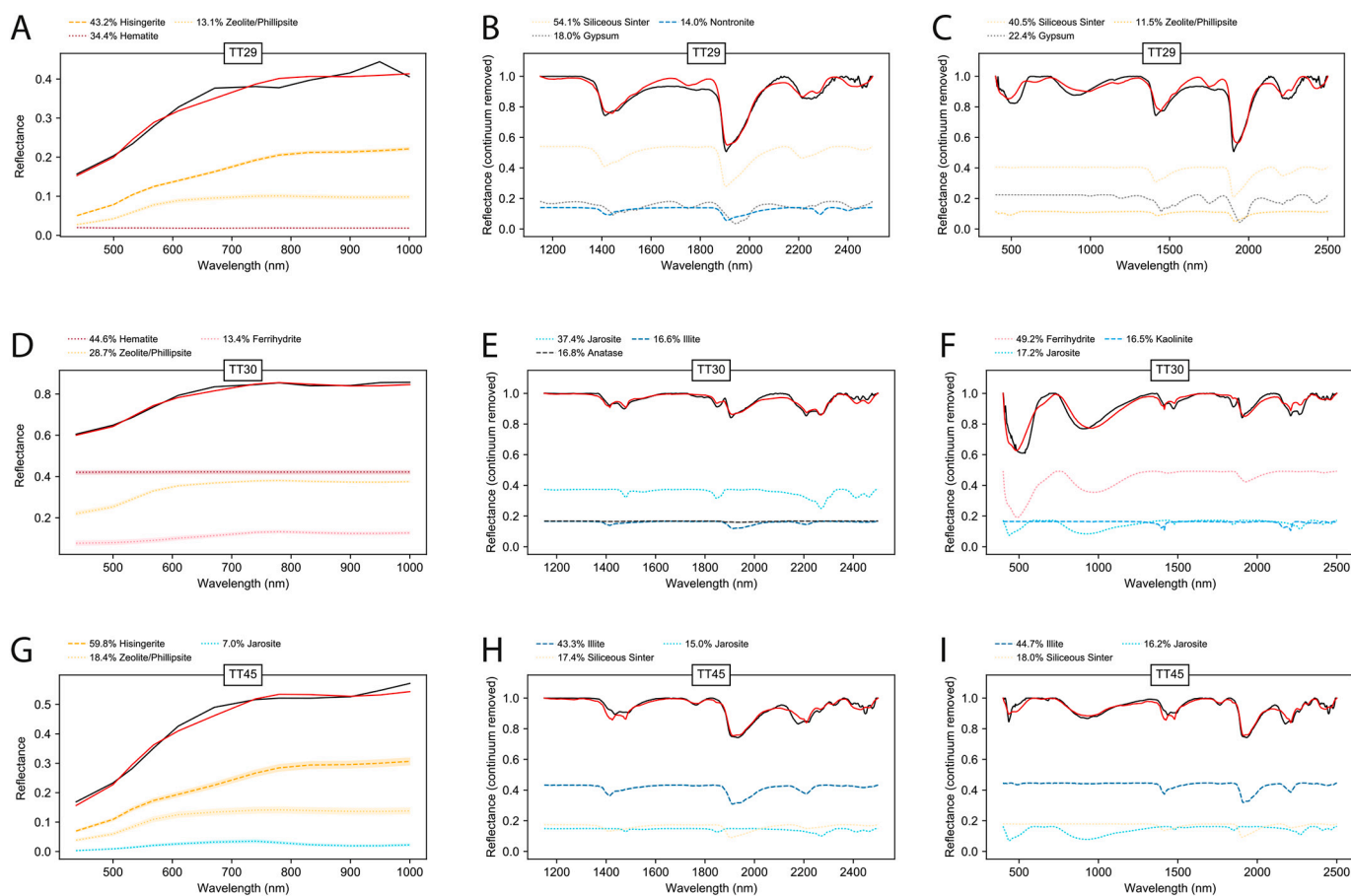

Fig. 14. Monte Carlo Markov Chain fitting results for Targets TT29 (A-C), TT30 (D–F), TT45 (G-I). Only the top three contributing endmembers are plotted. Each row corresponds to a single target, while each column represents the AUPE3, ISEM-E, and extended wavelength ranges respectively. For all plots black lines show the input spectrum, and red lines show the fitted output spectrum. Median fit coefficients are plotted for each endmember, surrounding shaded regions show the 15th and 85th percentile boundaries. For each AUPE3 input spectrum error bars are shown for each filter. Error bars for ISEM-E spectra are too small to be plotted. (For interpretation of the references to color in this figure legend, the reader is referred to the web version of this article.)

color imagery (i.e. CaSSIS, HRSC). We show that ground-based spectral observations from AUPE3 and ISEM-E provide fine-scale spectral and spatial insight into features like alteration gradients that cannot be observed at a significantly coarser spatial resolution in aerial imagery (e. g. Figs. 3 and 6). While previous rover-based missions (e.g. NASAs

Curiosity) have a history of "ground-truthing" spectral observations observed from orbit, ExoMars' ISEM instrument (along with the Mars2020 Supercam) will have the ability to ground-truth SWIR orbital observations at hyperspectral resolution.

In the SWIR, we note some discrepancies between aerial and ground-

Table 2

Summary of target results for the multi-scale analysis of the fumarole transect. Asterisks in the MCMC columns indicate poor fits. The full suite of contributing endmembers for each target are given in the Supplementary Information.

Target	AUPE3	ISEM-E	Raman	XRF (>median wt %)	AUPE3 MCMC (Top 3 Endmembers)	ISEM-E MCMC (Top 3 Endmembers)	Extended MCMC (Top 3 Endmembers)
TT26	Hematite	Silica/kaolinite, potentially more crystalline than majority targets	Anatase	Fe, Al, Mg, Ca	*Hematite, ferrihydrite, hisingerite*	Hydrated silica, illite, kaolinite	Hydrated silica, goethite, kaolinite
TT27	Hematite, jarosite, (Fe^{3+})	Poorly crystalline silica/Al-phase, deep OH & H_2O features	Anatase	Fe, Al, Mg, Ca	Hematite, jarosite, goethite	Hydrated silica, *gypsum*, nontronite	Hydrated silica, gypsum, ferrihydrite
TT28	Hematite	Poorly crystalline silica/Al-phase	Anatase	Mg, Ca, Si	*Hematite, hisingerite, zeolite*	Hydrated silica, hisingerite, ferrihydrite	Hydrated silica, illite, anatase
TT29	Hematite	Poorly crystalline silica/Al-phase, deep OH & H_2O features	Anatase	Ti, Si	*Hisingerite*, hematite, zeolite	Hydrated silica, *gypsum, nontronite*	Hydrated silica, *gypsum*, zeolite
TT30	Hematite, jarosite, (Fe^{3+})	Jarosite, Al-OH doublet	Anatase, Ca-heulandite	Al, Mg, Ca, Ti, Si	Hematite, zeolite, ferrihydrite	Jarosite, anatase, illite	Ferrihydrite, jarosite, kaolinite
TT31	Hematite, jarosite, (Fe^{3+})	Poorly crystalline silica/Al-phase, potentially more crystalline than majority targets	Anatase	Ti, Si	Hisingerite, zeolite, ferrihydrite	Illite, zeolite, goethite	Ferrihydrite, hydrated silica, illite
TT32	Hematite, jarosite, (Fe^{3+})	Poorly crystalline silica/Al-phase	Anatase, Gyspum	Fe, Al, Ti, Si	Hisingerite, ferrihydrite, jarosite	Hydrated silica, *hematite*, zeolite	Hydrated silica, *ferrihydrite*, zeolite
TT33	Hematite, jarosite, (Fe^{3+})	Poorly crystalline silica/Al-phase	Anatase, Gypsum	Ti, Si	Hisingerite, zeolite, hematite	Hydrated silica, hematite, jarosite	*Ferrihydrite, hydrated silica, gypsum*
TT35	Goethite	Poorly crystalline silica/Al-phase	Anatase	Ti, Si	Illite, zeolite, ferrihydrite	Hydrated silica, hematite, zeolite	Hydrated silica, montmorillonite, hematite
TT36	Hematite, jarosite, (Fe^{3+})	Poorly crystalline silica/Al-phase, deep OH & H_2O features	Anatase	Ti, Si	Hydrated silica, illite, hematite	Hydrated silica, montmorillonite, gypsum	*Ferrihydrite, gypsum, zeolite*
TT43	Hematite	Poorly crystalline silica/Al-phase	N/A	N/A	Zeolite, hisingerite, illite	Hydrated silica, hisingerite, szomolnokite	Illite, hydrated silica, jarosite
TT45	Hematite, Fe-basalt, (Fe^{2+})	Jarosite, Al-OH doublet, potentially more crystalline than majority targets	N/A	N/A	Hisingerite, zeolite, jarosite	Illite, hydrated silica, jarosite	*Hydrated silica, ferrihydrite, hisingerite*
TT48	Goethite	Poorly crystalline silica/Al-phase	N/A	Fe, Al, Mg, Ca	*Hematite, ferrihydrite, zeolite*	Hydrated silica, zeolite, goethite	Hydrated silica, geothite, szomolnokite
TT49	Fe-basalt, (Fe^{2+})	Poorly crystalline silica/Al-phase	N/A	Fe, Al, Mg, Ca	*Hematite, ferrihydrite, zeolite*	Hydrated silica, hisingerite, montmorillonite	Hydrated silica, hisingerite, montmorillonite

based spectra at our study site. Spectra from our aerial dataset are heavily affected by atmospheric and liquid water. When the aerial dataset was collected in September 2008, Iceland was experiencing higher than average precipitation (Icelandic Met Office, 2009). Although the FLAASH atmospheric correction was applied in our pre-processing, additional surface moisture resulting from heavy precipitation has meant that the size of the absorption band at ~1900 nm masks any absorption features expected at ~2200 nm. If any such features were present, their amplitude would be reduced as a consequence of the increased moisture content of the soil (Bowers and Hanks, 1965), as such, these features are obscured by signal noise. For example, in the ISEM-E spectrum in Fig. 2 we see a broad absorption feature around ~2200 nm with weak absorptions near 2210 and 2260 nm indicative of poorly crystalline silica. In the aerial fumarole spectrum, the absorption around ~1900 nm is so large that it overlaps the ~2200 nm region and obscures any potential features. In this figure we see that aerial spectra also possess lower signal-to-noise values than ISEM-E, and weak absorption features are not discernible in the ~2200 nm region. The high moisture content of the aerial scene is also apparent in the overall negative slope of its spectra (Fig. 2) as an overall decrease in albedo correlates with soil moisture content (Wu et al., 2009).

Martian datasets will not be affected by atmospheric water signatures; rather, ISEM will capture rover-based SWIR hyperspectral signatures free from the influence of Mars CO_2 atmosphere which can be used to constrain atmospheric correction algorithms and improve the accuracy of orbital information. Some atmospheric CO_2 contributions may faintly affect the 2000 nm region of ISEM data when working distances are larger (>4 m), but to a far lesser extent than is observed in CRISM observations.

4.2. Comparison of AUPE3 spectra with ISEM-E

Discrepancies were identified between AUPE3 and overlapping ISEM-E "extended range" spectra for the 530 nm slope (observed in the ISEM-E data) and in the incorrect differentiation between hematite and goethite (e.g. target TT48) in Fig. 5. For multiple AUPE3 targets the broad 900 nm feature observed by ISEM-E was suppressed (e.g. target TT30) and a downturn from 950 to 1000 nm which can be consistent with hydration state feature was not present (e.g target TT27). These may be a result of stray light effects known to exist in the AUPE3 system (Harris et al., 2015), however, for AUPE3 typically only image edges are affected. It is more likely that these discrepancies arise from differences in AUPE3 ROI content compared to the content captured within the smaller footprint of ISEM-E. Firstly, for example, in Fig. 5-A the AUPE3 spectrum for target TT36 is more consistent with its visible color gradient in Fig. 5-B, while the ISEM-E spectrum possesses more dramatic absorption features. As Fig. 5-B contains multiple float rocks of varying sizes it's possible that some of these larger floats could conceal smaller, more diverse pebbles which are captured in the 1 cm FOV of ISEM-E while it's held to the ground. Within this small footprint, ISEM-E would also be more sensitive to point-to-point variation than AUPE3. Secondly, while AUPE3 ROIs were created to match as closely as possible the ISEM-E sampling footprint on the ground they may contain one or two additional pixels from the surrounding region, affecting the ROI average spectrum. These effects are also responsible for the mismatches between AUPE3 and ISEM-E spectra in Fig. 9. We see in Fig. 9-D that the AUPE3 data separates into Fe-rich and Si-rich regions corresponding to the fumarole edges and center respectively, but in the ISEM-E verification data (Fig. 9-E) no such separation is observed. Here, target TT36 possesses large band depths at ~500 and 900 nm, conversely, in

the AUPE3 plot it possesses the smallest. The two emulators are again observing two different scales, with AUPE3 capturing the fumarole scale alteration gradient and ISEM-E capturing alteration at the sub-cm level within this gradient. The PanCam and ISEM flight instruments are co-located on *Rosalind Franklin's* mast and will not experience these footprint variations. Finally, there is a difference in measurement geometry between AUPE3 and ISEM-E which likely makes a small contribution to the differences between AUPE3 and ISEM-E spectra. AUPE3 is observing diffusely illuminated targets from a relatively high emission angle (hemispherical/directional measurement geometry), while ISEM-E is observing the targets with directional/directional geometry with a small phase angle.

We find that sub-meter spectral diversity at our field site can be effectively approximated using AUPE3 PCA results alone – samples at the extremities of the PCA plot (Fig. 7) represent soils with different color characteristics across the alteration gradient, indicative of chemical leaching differences. In Fig. 7-B, we show that PCA can be performed with only the LWAC RGB filters (3 filters), rather than the full geological filter suite (12 filters) to capture scene diversity. This is because the RGB filters contribute most to the largest principal components. For ExoMars, this finding is beneficial as it could reduce data volume requirements for PanCam; however, it comes with the caveat that the martian environment will have a strong influence on what filters are best to use over the course of *Rosalind Franklin's* traverse. As martian dust is strongly absorbing across much of the visible wavelength range and slightly forward scattering at longer NIR wavelengths (Bell et al., 2000), filters in the NIR may have a distinct advantage in surveying for underlying spectral variability in many terrains, depending on dust cover. We find that scene-selected endmembers from dimensionality reduction techniques such as PCA or MNF (or from decorrelation stretching (Fig. 4-C)) can provide an efficient means to locate pixels with similar geochemical properties in a image or image set (Fig. 8-B). Scene-selected endmembers also offer an advantage in that classification results do not rely on pre-constructed reference libraries. Pre-constructed libraries, like the RELAB subset library used in this work, provide an effective means of identifying and visualizing mineral phases within an image but limit the "discovery" of minerals to those within the library, and risk the identification of false-positives.

From the MCMC results in Fig. 13, we observed a difference in Fe content between AUPE3 and ISEM-E datasets. The AUPE3 plot in Fig. 13-A shows that the contributions of Fe-bearing phases are large for targets at the fumarole edges, and decrease approaching the center. This is consistent with fumarolic alteration patterns described by Carson (2015) and Markússon and Stefánsson (2011). However, ISEM-E and extended wavelength results record very little Fe contribution toward the fumarole edges, and greater contributions toward the center. We initially attributed this discrepancy to the fact that AUPE3 wavelength range is able to observe the left wing of the Fe absorption centered around 1000 nm, while the ISEM-E data doesn't record this feature. However, the extended range data (350–2500 nm) does, and it also shows higher Fe contributions toward the fumarole center. We consulted the fit results for TT32 (see Supplementary Information), which has large contributions from Fe-bearing phases in both ISEM-E and extended wavelength ranges in Fig. 13-BC, and found that while the wavelength range near 1000 nm had been poorly fit, the fit of the overall spectrum had been optimized by the algorithm. This issue was seen to occur to varying degrees across all wavelength ranges (AUPE3, ISEM-E, and extended range) and resulted in a bias in endmember contributions dependent on wavelength range.

As another example of an MCMC fitting discrepancy, we suspect that gypsum was selected as a contributing endmember to TT29 as its inclusion broadens the 1900 nm absorption feature of the fit spectrum (red in Fig. 14-BC) and approximates the noisy and shallow band depth present in the target spectrum around 2450 nm (black in Fig. 14-BC). However, Raman results (Fig. 12) show that gypsum is not observed in TT29, only in TT32 and TT33. The MCMC algorithm has therefore fitted gypsum as an endmember in its linear mixing model to approximate some, but not all, features of the target spectrum. As a result the 1800 nm band consistent with gypsum has been modeled in the fit spectrum for TT29 (Fig. 14-BC) when this feature isn't present in the target spectrum. We therefore interpreted the plots produced by the MCMC algorithm (Fig. 13) cautiously, and in combination with their fit results in Fig. 14. In the Supplementary Information we provide results and uncertainties for all transect targets across AUPE3, ISEM-E and extended (438–2500 nm) ranges. MCMC spectral fitting is a useful tool to provide insight into the potential endmember contributions for each spectrum and could prove to be a strong technique for implementation on Exo-Mars PanCam and ISEM data. However, additional work is needed to quantify the errors and uncertainties associated with the endmember contributions it provides, preferably using analog mixtures relevant to planetary surfaces (as in Lapotre et al. (2017)). Studies quantifying the effect of supplying linear vs non-linear posterior probability functions to MCMC unmixing techniques should also be undertaken using planetary analog soils. In advance of the ExoMars surface mission, refined MCMC approaches could also be tested on MSL Mastcam and ChemCam (Wiens et al., 2012) passive spectra to confirm if this technique allows for good agreement with CheMin-XRD (Blake et al., 2012) and/or APXS (Gellert et al., 2009) geochemistry results from the martian surface.

4.3. Inferring geochemistry with AUPE3 and ISEM-E

Comparing our spectral composition results with the true and false color maps in Figs. 3 and 4 and XRF results (Fig. 11) we find (like Mínguez et al. (2011)) that the changes in color across the fumarole apron related to changes in the broad underlying geochemistry. The combination of AUPE3 multispectral imaging and ISEM-E point spectra specifically reveal the fumarole alteration gradient to be comprised of unconsolidated sediments including (i) Al-OH minerals, (ii) hydrated silica, (iii) sulfates, and (iv) a variety of ferric oxides (Table 2).

When the fumaroles at the Hverir geothermal site were active, hydrogen sulfide gases interacted with the basaltic substrate to produce acid-sulfate waters enriched in H_2SO_4, Fe, and Al (Carson, 2015). These acid-sulfate waters reacted with the surrounding basaltic substrate to produce secondary mineral assemblages dominated by hydrated silica, Al/Fe-sulfates, Al-OH materials (i.e. Al-clays), and Fe-oxides. The bulk composition of alteration products at our study site is therefore controlled by leaching and mobilization of major elements (e.g. Fe, Al, Ca, Mg) out of the deposits, leaving Si relatively enriched (Fig. 11 & Table 2). This process occurs along a gradient based on distance from the fumarole center (Carson, 2015; Markússon and Stefánsson, 2011; Hynek et al., 2013). Precipitation of secondary Fe-bearing minerals, to which AUPE3 and PanCam are particularly sensitive, within this fumarole environment is highly dependent on pH, sulfate, and Fe concentration (Farrand et al., 2009). Phases likely to form from low-pH, sulfate-rich fluids near the fumarole center are jarosite and goethite. In terrestrial systems jarosite is relatively unstable, breaking down to form Fe^{3+} oxides and hydroxides such as hematite or goethite, depending on the environmental conditions (Carson, 2015). AUPE3 spectral data (Fig. 3) identifies hematite at the edges of the apron and ferrihydrite, alunite and jarosite approaching fumarole center (Fig. 13. The fact that we observe jarosite at this fumarole indicates that extinction happened fairly recently in geological time as jarosite can be used as an indicator to gauge the extent of chemical weathering – jarosite can only form and remain stable if the alteration process is halted during the early stages of basaltic weathering (Elwood Madden et al., 2004). As the Hverir lava field is estimated to be ~10,000 years old (Carson, 2015), and sub-aerial weathering processes are slow in Iceland due to a lack of rainfall, the jarosite has not yet been removed by the effects of post-emplacement subaerial weathering. The fact that we observe localized patches of fumarolic alteration material among a region of unaltered primary basalt (Fig. 1-CG) also suggests that sub-aerial weathering was not a driving factor in the production of the alteration phases at our study site.

On Mars, at Oxia Planum *Rosalind Franklin* will observe clay-rich deposits produced in part by ancient (~3.8 Ga) sub-aerial weathering processes, however, since the Late Noachian the lack of water stability at Mars' surface has meant that little evidence has been found for the modern chemical alteration of martian soils (Yen et al., 2005).

Hydrated (opaline) silica is a common alteration product formed through aqueous interaction with basalt, and has been detected in several localities on Mars both via orbital (Sun and Milliken, 2018) and ground-based measurements (Squyres et al., 2008; Rice et al., 2010), most recently in Jezero Crater (Tarnas et al., 2019). We find that the increased silica content toward the fumarole center limits the ability of ISEM-E to distinguish spectral features associated with Al-OH and kaolin group minerals due to a broadening of the ~2200 nm feature. However, XRF elemental results show that targets rich in major elements are found toward the edges of the fumarole, while Si rich targets are found toward the center. For ExoMars, spatially-fine VNIR/SWIR spectral data from MicrOmega (Bibring et al., 2017) will facilitate discrimination between these alteration phases at the micron-to-mm scale.

Hynek et al. (2013) and Carson (2015) show that amorphous silica is produced as the dominant alteration product from active fumarolic systems that have not yet weathered. To investigate the relative crystallinity of alteration phases within our targets we used the ~1400 nm feature; previously demonstrated by Sun and Milliken (2018) to shift to shorter wavelengths (<1420 nm) for amorphous silica and to longer wavelengths (>1410 nm) for more crystalline phases. Plotting this 1400 nm band position against the 2260/2210 nm band depth ratio we showed (Fig. 10) that all our targets contain poorly crystalline, rather than truly amorphous materials, as they represent intermixed alteration phases from a fumarole-driven environment rather than pure samples. Ground-based ISEM-E and remote aerial detection of Al-OH and Si-OH SWIR absorption bands (Figs. 3 and 6-A) likewise point to poorly crystalline intermixed phases within their respective FOV.

4.4. Implications for ExoMars 2022

From Table 2 we see that although hydrated silica and hematite were observed in VNIR and SWIR datasets, we did not detect evidence for these phases during Raman analysis. This may be because Raman point analysis only covers a very small FOV (50 μm) and multiple analyses must be carried out in order to detect all phases present within a target sample; the RLS onboard *Rosalind Franklin* will analyze between 20 and 39 spots per target and is equipped with high-resolution grid mapping capabilities to ensure thorough target coverage (Veneranda et al., 2020). Conversely, we identified anatase with Raman in every target sample taken across the fumarole transect. Raman is overly sensitive to Ti-oxides, in addition to Fe-oxides and sulfur, which can overwhelm the signal and mask the detection of other phases (Black and Hynek, 2018). Anatase was only observed in ISEM-E SWIR spectral data through MCMC fitting (Fig. 13) and likely as a result of overfitting as the anatase spectrum is relatively featureless in the SWIR. Raman is also not ideal for the identification of phyllosilicates or amorphous materials, such as opaline silica, as these can fluoresce strongly (Black and Hynek, 2018). To mitigate these effects in the phyllosilicate-rich environment at Oxia Planum, ExoMars' RLS data will be cross-correlated with VNIR and SWIR data from MicrOmega (500–3650 nm) (Bibring et al., 2017) which is co-located with RLS, as well as PanCam and ISEM to ensure successful identification of molecules, minerals, and rocks Rull et al. (2017).

In Fig. 8-B, dark-toned float rocks toward the center of the fumarole were classified along with "light soils" using AUPE3 endmembers selected from within the scene. This is because the SAM classifier is insensitive to illumination effects, however, we see from this figure that it can also be beneficial to incorporate absolute differences in reflectance alongside spectral shape. For improved discrimination a greater number of scene-selected endmembers could be created for specific targets of interest or an alternative classification method could be used that simply assigns each target spectrum to its closest endmember in vector space. It is worth noting that on Mars, direct and diffuse lighting components will contribute spectrally distinct illumination to targets which may confuse any supervised classifier on heavily shaded rock facets.

Operating instruments in the martian environment will pose challenges for analysis of spectral data as all of the terrain will have a covering of Fe-rich dust. The primary remote-sensing instruments on *Rosalind Franklin*, PanCam and ISEM, will rely on observations of a radiometric calibration target to generate data products like reflectance from which true color imagery and spectral parameter maps are derived. However, dust deposition on the calibration target will alter the reflectance of its patches, making measurements of the solar illumination – and therefore of any derived data products – progressively less accurate. NASA/JPL camera teams have overcome this problem by developing a radiative transfer model to calculate the reflectance of the dust-covered calibration targets, allowing them to correct for the dust (Bell et al., 2006; Johnson et al., 2006; Kinch et al., 2007, 2015). We, and members of the PanCam Science Team, are currently building on these studies to characterize, and compensate for, the incident solar illumination spectrum and airborne and deposited dust that PanCam will encounter. This work will result in derived data products such as true color imagery, false color and enhanced imagery, and accurate reflectance measurements (including uncertainty) so that interpretation of additional derived products, like spectral reflectance maps (e.g. Fig. 3), can be undertaken with confidence.

5. Conclusions

The fumarole alteration sediments at Námafjall display a diversity of hydrothermal alteration phases across the meter-to-micron scale. We explored multiple methods for discriminating between these intermixed, poorly crystalline phases using imagery and VNIR/SWIR spectra provided by the ExoMars 2022 remote-sensing emulator suite (AUPE3, ISEM-E, CLUPI-E) in combination with aerial VNIR/SWIR data and lab-based analyzes (XRF, Raman). This work is key in determining instrument capabilities and inter-instrument cohesion for ExoMars 2022 remote-sensing payload before launch in 2022.

We found that:

1. Eagle/Hawk aerial observations in combination with AUPE3 mosaics provided local-to-regional snapshots of spectral variability. Using the spectral summary products created for CRISM (Pelkey et al., 2007; Viviano-Beck et al., 2014) and for PanCam (Harris et al., 2015; Allender et al., 2020) we characterized the mineralogy of meter scale alteration patterns with true/false color mosaics and spectral parameter mosaics.
2. AUPE3 was able to visualize sub-meter spectral diversity across hydrothermally altered basaltic terrain and capture the transition from Fe-rich sediments at the fumarole edges to the silica-rich material at fumarole center. We found some discrepancies between AUPE3 and handheld ISEM-E observations that stem from differences in emulator FOV and recommend further studies are undertaken with a mounted ISEM-E before ExoMars' launch.
3. Spectral variability was captured effectively by performing PCA on AUPE3's three narrow-band RGB filters, rather than the full 12-filter geology suite. This could reduce data volume requirements for PanCam tactical observations, however, dust coverage at the martian surface will strongly influence the filter subsets selected over the course of *Rosalind Franklin's* traverse.
4. Raman and SWIR ISEM-E data are not able to be cross-referenced for intermixed sediments as scale differences are too large. For ExoMars, RLS will be co-located with MicrOmega which will provide SWIR data at a comparable scale (50 μm) with multiple target measurements.
5. While SWIR spectral ratios and parameter spaces can be used to infer the crystallinity of dominant phases, ISEM-E cannot discriminate

between poorly crystalline Al-OH and amorphous Si-OH phases in intermixed sediments.

6. Observing spectral and geochemical relationships is inherently difficult in intermixed, poorly crystalline sediments. XRF data recorded the strongest evidence for chemical leaching across the fumarole alteration gradient, however, due to the dominance of the 2200 nm spectral feature consistent with hydrated silica, no clear relationship was able to be observed between the position of SWIR metal-OH bands recorded by ISEM-E and the underlying target chemistry provided by XRF.

7. Monte Carlo Markov Chain spectral fitting is a useful technique to identify endmember contributions within poorly crystalline, intermixed sediments; however, additional studies are required to quantify and constrain the accuracy of its retrievals.

8. The bulk composition of alteration products at the Hverir geothermal field is controlled by leaching and mobilization of major elements (e. g. Fe, Al, Ca, Mg) out of the deposits, leaving Si relatively enriched. This process occurs along a gradient based on distance from the fumarole center. We observed hematite, goethite, jarosite, kaolinite, gypsum, hydrated silica, and anatase at multiple scales across the fumarole gradient using the ExoMars remote-sensing emulator suite.

Declaration of Competing Interest

None.

Acknowledgments

Appendix A. Supplementary data

Supplementary data to this article can be found online at https://doi. org/10.1016/j.icarus.2021.114541.

References

Alexander, D.A., Deen, R.G., Andres, P.M., Zamani, P., Mortensen, H.B., Chen, A.C., Cayanan, M.K., Hall, J.R., Klochko, V.S., Pariser, O., Stanley, C.L., Thompson, C.K., Yagi, G.M., 2006. Processing of Mars Exploration Rover imagery for science and operations planning. J. Geophys. Res. 111 https://doi.org/10.1029/2005JE002462.

Allender, E., Stabbins, R., Gunn, M., Cousins, C., Coates, A., 2018. The ExoMars Spectral Tool (ExoSpec): an image analysis tool for ExoMars 2020 PanCam imagery. In: Image and Signal Processing for Remote Sensing, XXIV. https://doi.org/10.1117/12.2325659.

Allender, E., Cousins, C., Gunn, M., Caudill, C., 2020. Multiscale and multispectral charazterization of mineralogy with the ExoMars 2022 rover remote sensing payload. Earth Space Sci. 7, 1–18. https://doi.org/10.1029/2019EA000692.

Barnes, D., Wilding, M., Gunn, M., Medwyn Pugh, S., Gethyn Tyler, L., Coates, A., Griffiths, A.R., Cousins, C., Schmitz, N., Bauer, A., Paar, G., 2011a. Multi-spectral vision processing for the ExoMars 2018 mission. In: 11th Symposium on Advanced Space Technologies in Robotic and Automation (ASTRA 2012).

Barnes, D., Wilding, M., Gunn, M., Tyler, L., Pugh, S., Coates, A., Griffiths, A., Cousins, C., Schmitz, N., Paar, G., 2011b. The PanCam Calibration Target (PCT) and multispectral image processing for the ExoMars 2018 mission. In: EPSC-DPS Joint Meeting 2011, p. 289.

Bell, J.F., McSween, H.Y., Crisp, J.A., Morris, R.V., Murchie, S.L., Bridges, N.T., Johnson, J.R., Britt, D.T., Golombek, M.P., J, M.H., Ghosh, A., Bishop, J.L., Anderson, R.C., Brückner, J., Economou, T., Greenwood, J.P., Gunnlaugsson, H.P., Hargraves, R.M., Hviid, S., Knudsen, J.M., Madsen, M.B., Reid, R., Rieder, R., Soderblom, L., 2000. Mineralogic and compositional properties of Martian soil and dust: Results from Mars Pathfinder. J. Geophys. Res. Planets 105, 1721–1755. https://doi.org/10.1029/1999JE001060.

Bell, J., Joseph, J., Sohl-Dickstein, J., 2004. MER Pancam Data Processing User's Guide, 1.0 ed. Cornell University. URL: https://pds-imaging.jpl.nasa.gov/data/mer/opport unity/mer1po_0xxx/document/pancam_users_guide.pdf.

Bell, J.F., Squyres, S.W., Arvidson, R.E., Arneson, H.M., Bass, D., Blaney, D., Cabrol, N., Calvin, W., Farmer, J., Farrand, W.H., Goetz, W., Golombek, M., Grant, J.A., Greeley, R., Guinness, E., Hayes, A.G., Hubbard, M.Y.H., Herkenhoff, K.E., Johnson, M.J., Johnson, J.R., Joseph, J., Kinch, K.M., Lemmon, M.T., Li, R., Madsen, M.B., Maki, J.N., Malin, M., McCartney, E., McLennan, S., McSween, H.Y., Ming, D.W., Moersch, J.E., Morris, R.V., Dobrea, E.Z.N., Parker, T.J., Proton, J., Rice, J.W., Seelos, F., Soderblom, J., Soderblom, L.A., Sohl-Dickstein, J.N., Sullivan, R.J., Wolff, M.J., Wang, A., 2004b. Pancam multispectral imaging results from the Spirit rover at Gusev Crater. Science 305, 800–806. https://doi.org/10.1126/science.1100175.

Bell, J.F., Squyres, S.W., Arvidson, R.E., Arneson, H.M., Bass, D., Calvin, W., Farrand, W. H., Goetz, W., Golombek, M., Greeley, R., Grotzinger, J., Guinness, E., Hayes, A.G., Hubbard, M.Y.H., Herkenhoff, K.E., Johnson, M.J., Johnson, J.R., Joseph, J., Kinch, K.M., Lemmon, M.T., Li, R., Madsen, M.B., Maki, J.N., Malin, M., McCartney, E., McLennan, S., McSween, H.Y., Ming, D.W., Morris, R.V., Dobrea, E.Z. N., Parker, T.J., Proton, J., Rice, J.W., Seelos, F., Soderblom, J.M., Soderblom, L.A., Sohl-Dickstein, J.N., Sullivan, R.J., Weitz, C.M., Wolff, M.J., 2004c. Pancam multispectral imaging results from the Opportunity rover at Meridiani Planum. Science 306, 1703–1709. https://doi.org/10.1126/science.1105245.

Bell, J.F., Joseph, J., Sohl-Dickstein, J.N., Arneson, H.M., Johnson, M.J., Lemmon, M.T., Savransky, D., 2006. In-flight calibration and performance of the Mars Exploration Rover Panoramic Camera (Pancam) instruments. J. Geophys. Res. Planets 111. https://doi.org/10.1029/2005JE002444.

Bell, J., Maki, J., Mehall, G., Ravine, M., Caplinger, M., the Mastcam-Z Team, 2016. Mastcam-Z: Designing a geologic, stereoscopic, and multispectral pair of zoom cameras for the NASA Mars 2020 rover. In: 3rd International Workshop on Instrumentation for Planetary Missions. Abstract 4126.

Bibring, J.P., Hamm, V., Pilorget, C., Vago, J.L., the MicrOmega Team, 2017. The MicrOmega Investigation Onboard ExoMars. Astrobiology 17, 621–626. https://doi.org/10.1089/ast.2016.1642.

Bish, D.L., Blake, D.F., Vaniman, D.T., Chipera, S.J., Morris, R.V., Ming, D.W., Treiman, A.H., Sarrazin, P., Morrison, S.M., Downs, R.T., Achilles, C.N., Yen, A.S., Bristow, T.F., Crisp, J.A., Morookian, J.M., Farmer, J.D., Rampe, E.B., Stolper, E.M., Spanovich, N., Science Team, M.S.L., 2013. X-ray Diffraction Results from Mars Science Laboratory: Mineralogy of Rocknest at Gale Crater. Science 341. https://doi.org/10.1126/science.1238932.

Bishop, J.L., 2018. Chapter 3 - Remote detection of phyllosilicates on Mars and implications for climate and habitability. In: Cabrol, N.A., Grin, E.A. (Eds.), From Habitability to Life on Mars. Elsevier, pp. 37–75. https://doi.org/10.1016/B978-0-12-809,935-3.00003-7.

Bishop, J., Lane, M., Dyar, M., Brown, A., 2008. Reflectance and emission spectroscopy study of four groups of phyllosolicates: smectites, kaolinite-serpentines, chlorites and micas. Clay Miner. 43, 35–54. https://doi.org/10.1180/claymin.2008.043.1.03.

Black, S., Hynek, B., 2018. Characterization of terrestrial hydrothermal alteration products with Mars analog instrumentation: Implications for current and future rover investigations. Icarus 307, 235–259. https://doi.org/10.1016/j.icarus.2017.10.032.

Blake, D., Vaniman, D., Achilles, C., Anderson, R., Bish, D., Bristow, T., Chen, C., Chipera, S., Crisp, J., Des Marais, D., Downs, R.T., Farmer, J., Feldman, S., Fonda, M., Gailhanou, M., Ma, H., Ming, D.W., Morris, R.V., Sarrazin, P., Stolper, E., Treiman, A., Yen, A., 2012. Characterization and calibration of the chemin mineralogical instrument on mars science laboratory. Space Sci. Rev. 170, 341–399. https://doi.org/10.1007/s11214-012-9905-1.

Bowers, S., Hanks, R., 1965. Reflection of radiant energy from soils. Soil Sci. 100, 130–138. https://doi.org/10.1097/00010694-196,508,000-00009.

Carson, G., 2015. Hydrothermal acid-sulfate alteration at Krafla and Námafjall, NE Iceland: implications for Gusev Crater and Meridiani Planum, Mars. Master's thesis. University of Wisconsin-Milwaukee. URL: https://dc.uwm.edu/etd/797. paper 797.

Clark, R., 1999. Chapter 1: spectroscopy of rocks and minerals and principles of spectroscopy. In: Remote Sensing for the Earth Sciences: Manual of Remote Sensing, , 3 edvol. 3. John Wiley and Sons Inc.

Coates, A., Jaumann, R., Griffiths, A., Leff, C., Schmitz, N., Josset, J.L., Paar, G., Gunn, M., Hauber, E., Cousins, C., Cross, R., Grindrod, P., Bridges, J., Balme, M., Gupta, S., Crawford, I., Irwin, P., Stabbins, R., Tirsch, D., Vago, J., Theodorou, T., Caballo-Perucha, M., Osinski, G., the PanCam Team, 2017. The PanCam instrument for the ExoMars rover. Astrobiology 17, 511–541. https://doi.org/10.1089/ast.2016.1548.

Cousins, C., Gunn, M., Prosser, B., Barnes, D., Crawford, I., Griffiths, A., Davis, L., Coates, A., 2012. Selecting the geology filter wavelengths for the ExoMars Panoramic Camera instrument. Planet. Space Sci. 71, 80–100.

Cuadros, J., Mavris, C., Michalski, J.R., Nieto, J.M., Bishop, J.L., Fiore, S., 2019. Abundance and composition of kaolinite on Mars: Information from NIR spectra of rocks from acid-alteration environments, Rio Tinto, SE Spain. Icarus 330, 30–41. https://doi.org/10.1016/j.icarus.2019.04.027.

Das, S., Hendry, M., Essilfie-Dughan, J., 2011. Transformation of two-line ferrihydrite to goethite and hematite as a function of ph and temperature. Environ. Sci. Technol. 45, 268–275. https://doi.org/10.1021/es101903y.

Dehouck, E., McLennan, S.M., Meslin, P.Y., Cousin, A., 2014. Constraints on abundance, composition, and nature of X-ray amorphous components of soils and rocks at Gale crater, Mars. J. Geophys. Res. Planets 119, 2640–2657. https://doi.org/10.1002/2014JE004716.

Dehouck, E., McLennan, S.M., Sklute, E.C., Dyar, M.D., 2017. Stability and fate of ferrihydrite during episodes of water/rock interactions on early mars: an experimental approach. J. Geophys. Res. Planets 122, 358–382. https://doi.org/10.1002/2016JE005222.

dos Santos, R., Patel, M., Cuadros, J., Martins, Z., 2016. Influence of mineralogy on the preservation of amino acids under simulated Mars conditions. Icarus 277, 342–353. https://doi.org/10.1016/j.icarus.2016.05.029.

Elwood Madden, M.E., Bodnar, R.J., Rimstidt, J.D., 2004. Jarosite as an indicator of water-limited chemical weathering on Mars. Nature 431, 821–823. https://doi.org/10.1038/nature02971.

Farrand, W., Bell, J., Johnson, J., Squyres, S., Soderblom, J., Ming, D., 2006. Spectral variability among rocks in visible and near-infrared multispectral Pancam data collected at Gusev crater: examinations using spectral mixture analysis and related techniques. J. Geophys. Res. 111. https://doi.org/10.1029/2005JE002495.

Farrand, W.H., Bell, J.F., Johnson, J.R., Arvidson, R.E., Crumpler, L.S., Hurowitz, J.A., Schröder, C., 2008. Rock spectral classes observed by the Spirit Rover's Pancam on the Gusev Crater Plains and in the Columbia Hills. J. Geophys. Res. 113. https://doi.org/10.1029/2008JE003237.

Farrand, W.H., Glotch, T.D., Rice, J.W., Hurowitz, J.A., Swayze, G.A., 2009. Discovery of jarosite within the Mawrth Vallis region of Mars: Implications for the geologic history of the region. Icarus 204, 478–488. https://doi.org/10.1016/j.icarus.2009.07.014.

Farrand, W.H., Bell, J.F., Johnson, J.R., Rice, M.S., Hurowitz, J.A., 2013. VNIR multispectral observations of rocks at Cape York, Endeavour crater, Mars by the Opportunity rover's Pancam. Icarus 225, 709–725. https://doi.org/10.1016/j.icarus.2013.04.014.

Farrand, W.H., Bell, J.F., Johnson, J.R., Rice, M.S., Jolliff, B.L., Arvidson, R.E., 2014. Observations of rock spectral classes by the Opportunity rover's Pancam on northern Cape York and on Matijevic Hill, Endeavour Crater, Mars. J. Geophys. Res. Planets 119, 2349–2369. https://doi.org/10.1002/2014JE004641.

Farrand, W., Johnson, J., Rice, M., Wang, A., Bell, J., 2016. VNIR multispectral observations of aqueous alteration materials by the Pancams on the Spirit and Opportunity Mars Exploration Rovers. Am. Mineral. 101, 2005–2019.

Fawdon, P., Balme, M., Bridges, J., Davis, J., Gupta, S., Sefton-Nash, E., Quantin-Nataf, C., The ExoMars RSOWG, 2020. Continuing characterization of Oxia Planum, the landing site for the ExoMars Rosalind Franklin rover. In: British Planetary Science Conference.

Gellert, R., Campbell, J., King, P., Leshin, L., Lugmair, G., Spray, J., Squyres, S., Yen, A., 2009. The Alpha-Particle-X-Ray-Spectrometer (APXS) for the Mars Science Laboratory (MSL) rover mission. In: Lunar and Planetary Science Conference XL. URL: https://www.lpi.usra.edu/meetings/lpsc2009/pdf/2364.pdf. abstract 2364.

Harris, J., Cousins, C., Gunn, M., Grindrod, P., Barnes, D., Crawford, I., Cross, R., Coates, A., 2015. Remote detection of past habitability at Mars-analogue hydrothermal alteration terrains using an ExoMars Panoramic Camera emulator. Icarus 252, 284–300. https://doi.org/10.1016/j.icarus.2015.02.004.

Herbert, R., 1997. Properties of goethite and jarosite precipitated from acidic groundwater, Dalarna, Sweden. Clay Clay Miner. 45, 261–273. https://doi.org/10.1346/CCMN.1997.0450214.

Hynek, B., McCollom, T., Marcucci, E., Brugman, K., Rogers, K., 2013. 2013. Assessment of environmental controls on acid-sulfate alterationat active volcanoes in Nicaragua: applications to relic hydrothermal systems on Mars. J. Geophys. Res. Planets 118, 2083–2104. https://doi.org/10.1002/jgre.20140.

Icelandic Met Office, 2009. The Weather in Iceland 2008. Online. URL: https://en.vedur.is/about-imo/news/nr/1438.

Johnson, J.R., Grundy, W.M., Lemmon, M.T., Bell, J.F., Johnson, M.J., Deen, R.G., Arvidson, R.E., Farrand, W.H., Guinness, E.A., Hayes, A.G., Herkenhoff, K.E., Seelos, F., Soderblom, J., Squyres, S., 2006. Spectrophotometric properties of materials observed by Pancam on the Mars Exploration Rovers: 1. Spirit. J. Geophys. Res. Planets 111. URL: https://agupubs.onlinelibrary.wiley.com/doi/abs/10.1029/2005JE002494, doi:10.1029/2005JE002494, arXiv: https://agupubs.onlinelibrary.wiley.com/doi/pdf/10.1029/2005JE002494.

Josset, J.L., Westall, F., Hofmann, B.A., Spray, J., Cockell, C., Kempe, S., Griffiths, A.D., De Sanctis, M.C., Colangeli, L., Koschny, D., Föllmi, K., Verrecchia, E., Diamond, L., Josset, M., Javaux, E.J., Esposito, F., Gunn, M., Souchon-Leitner, A.L., Bontognali, T. R., Korablev, O., Erkman, S., Paar, G., Ulamec, S., Foucher, F., Martin, P., Verhaeghe, A., Tanevski, M., Vago, J.L., 2017. The Close-Up Imager onboard the ESA ExoMars rover: objectives, description, operations, and science validation activities. Astrobiology 17, 595–611. https://doi.org/10.1089/ast.2016.1546.

Kinch, K.M., Sohl-Dickstein, J., Bell III, J.F., Johnson, J.R., Goetz, W., Landis, G.A., 2007. Dust deposition on the Mars Exploration Rover Panoramic Camera (Pancam) calibration targets. J. Geophys. Res. Planets 112. https://doi.org/10.1029/2006JE002807.

Kinch, K., Bell, J., Goetz, J., Johnson, J., Madsen, M., Sohl-Dickstein, J., 2015. Dust deposition on the decks of the Mars Exploration Rovers: 10 years of dust dynamics on the Panoramic Camera calibration targets. Earth Space Sci. 2, 144–172. https://doi.org/10.1002/2014EA000073.

King, O., Fletcher, L., 2020. Compositional mapping of Europa with VLT/SPHERE. In: British Planetary Science Conference, 67. URL: https://bpsc2020.files.wordpress.com/2020/03/bpsc2020_abstract_book_v3.pdf.

Knadel, M., Deng, F., Alinejadian, A., Wollesen de Jonge, L., Moldrup, P., Greve, M.H., 2014. The effects of moisture conditions–from wet to hyper dry–on visible near-infrared spectra of Danish reference soils. Soil Sci. Soc. Am. 78, 422–433. https://doi.org/10.2136/sssaj2012.0401.

Korablev, O.I., Dobrolensky, Y., Evdokimova, N., Fedorova, A.A., Kuzmin, R.O., Mantsevich, S.N., Cloutis, E.A., Carter, J., Poulet, F., Flahaut, J., Griffiths, A., Gunn, M., Schmitz, N., Martín-Torres, J., Zorzano, M.P., Rodionov, D.S., Vago, J.L., Stepanov, A.V., Titov, A.Y., Vyazovetsky, N.A., Trokhimovskiy, A.Y., Sapgir, A.G., Kalinnikov, Y.K., Ivanov, Y.S., Shapkin, A.A., Ivanov, A.Y., 2017. Infrared

spectrometer for ExoMars: a mast-mounted instrument for the rover. Astrobiology 17, 542–564. https://doi.org/10.1089/ast.2016.1543.

Kruse, F., Lefkoff, A., Boardman, J., Heidebrecht, K., Shapiro, A., Barloon, P., Goetz, A., 1993. The spectral image processing system (SIPS) – interactive visualization and analysis of imaging spectrometer data. Remote Sens. Environ. 44, 145–163. https://doi.org/10.1016/0034-4257(93)90013-N.

Lafuente, B., Downs, R., Yang, H., Stone, N., 2015. Highlights in Mineralogical Crystallography. W. De Gruyter. chapter The power of databases: the RRUFF project, pp. 1–30.

Lane, M., Morris, R.V., Christensen, P., 1999. Spectral behavior of hematite at visible/near infrared and mid infrared wavelengths. In: Fifth International Conference on Mars. Abstract 6085.

Lapotre, M.G.A., Ehlmann, B.L., Minson, S.E., 2017. A probabilistic approach to remote compositional analysis of planetary surfaces. J. Geophys. Res. Planets 122, 983–1009. https://doi.org/10.1002/2016JE005248.

Laurent, B., Cousins, C., Gunn, M., Huntly, C., Cross, R., Allender, E., 2019. UV luminescence characterization of organics in Mars-analogue substrates. Icarus 321, 929–937. https://doi.org/10.1016/j.icarus.2018.12.031.

Malin, M., Caplinger, M., Edgett, K., Ghaemi, F., Ravine, M., Schaffner, J., Baker, J., Bardis, J., DiBase, D., Maki, J., Willson, R., Bell, J., Deitrich, W., Edwards, L., Hallet, B., Herkenhoff, K., Heydari, E., Kah, L., Lemmon, M., Minitti, M., Olson, T., Parker, T., Rowland, S., Schieber, J., Sullican, R., Sumner, D., Thomas, P., Yingst, R., 2010. The Mars Science Laboratory (MSL) Mast-Mounted Cameras (Mastcams) Flight Instruments. In: 41st Lunar and Planetary Science Conference. Abstract 1123.

Markússon, S.H., Stefánsson, A., 2011. Geothermal surface alteration of basalts, Krýsuvík Iceland – Alteration mineralogy, water chemistry and the effects of acid supply on the alteration process. J. Volcanol. Geotherm. Res. 206, 46–59. https://doi.org/10.1016/j.jvolgeores.2011.05.007.

Martin, P.E., Ehlmann, B.L., Thomas, N.H., Wiens, R.C., Hollis, J.J.R., Beegle, L.W., Bhartia, R., Clegg, S.M., Blaney, D.L., 2020. Studies of a lacustrine-volcanic Mars analog field site with Mars-2020-like instruments. Earth Space Sci. 7 https://doi.org/10.1029/2019EA000720.

McNeil, J., Balme, M., Fawdon, P., Coe, A., 2020. The nature of remnant rounded mounds north of the ExoMars 2020 landing site. In: British Planetary Science Conference, p. 84. URL: https://bpsc2020.files.wordpress.com/2020/03/bpsc2020_abstract_book_v3.pdf.

McSween Jr., H.Y., McGlynn, I.O., Rogers, A.D., 2010. Determining the modal mineralogy of Martian soils. J. Geophys. Res. Planets 115. URL: https://agupubs.onlinelibrary.wiley.com/doi/abs/10.1029/2010JE003582, doi:10.1029/2010JE003582.

Michalski, J., Cuadros, J., Bishop, J., Darby Dyar, M., Dekov, V., Fiore, S., 2015. Constraints on the crystal-chemistry of Fe/Mg-rich smectitic clays on Mars and links to global alteration trends. Earth Planet. Sci. Lett. 427, 215–225. https://doi.org/10.1016/j.epsl.2015.06.020.

Mínguez, H., Ortega, L., Lunar, R., Martínez-Frías, J., Piña, R., 2011. Mineralogy of the Hydrothermal Alteration in the Námafjall Geothermal Field (Iceland), pp. 25–26.

Murchie, S.L., Seelos, F.P., Hash, C.D., Humm, D.C., Malaret, E., McGovern, J.A., Choo, T.H., Seelos, K.D., Buczkowski, D.L., Morgan, M.F., Barnouin-Jha, O.S., Nair, H., Taylor, H.W., Patterson, G.W., Harvel, C.A., Mustard, J.F., Arvidson, R.E., McGuire, P., Smith, M.D., Wolff, M.J., Titus, T.N., Bibring, J.P., Poulet, F., 2009. Compact Reconnaissance Imaging Spectrometer for Mars investigation and data set from the Mars Reconnaissance Orbiter's primary science phase. J. Geophys. Res. Planets 114. https://doi.org/10.1029/2009JE003344.

Parente, M., Bishop, J., Bell, J., 2009. Spectral unmixing for mineral identification in pancam images of soils in Gusev crater. Mars. Icarus 203, 421–436. https://doi.org/10.1016/j.icarus.2009.04.029.

Pelkey, S.M., Mustard, J.F., Murchie, S., Clancy, R.T., Wolff, M., Smith, M., Milliken, R., Bibring, J.P., Gendrin, A., Poulet, F., Langevin, Y., Gondet, B., 2007. CRISM multispectral summary products: parameterizing mineral diversity on Mars from reflectance. J. Geophys. Res. Planets 112. https://doi.org/10.1029/2006JE002831.

Poulet, F., Mangold, N., Loizeau, D., Bibring, J.P., Langevin, Y., Michalski, J., Gondet, B., 2008. Abundance of minerals in the phyllosilicate-rich units on Mars. A&A 487, L41–L44. https://doi.org/10.1051/0004-6361:200810150.

Quantin-Nataf, C., Thollot, P., Carter, J., Mandon, L., Dehouck, E., 2018. The unique and diverse record of Noachian aqueous activity in Oxia Planum, Mars. In: 49th Lunar and Planetary Science Conference. Abstract 2562.

Reid, R.J., Smith, P.H., Lemmon, M., Tanner, R., Burkland, M., Wegryn, E., Weinberg, J., Marcialis, R., Britt, D.T., Thomas, N., Kramm, R., Dummel, A., Crowe, D., Bos, B.J., Bell, J.F., Rueffer, P., Gliem, F., Johnson, J.R., Maki, J.N., Herkenhoff, K.E., Singer, R.B., 1999. Imager for Mars Pathfinder (IMP) image calibration. J. Geophys. Res. Planets 104, 8907–8925. https://doi.org/10.1029/1998JE900011.

Rice, M., Bell, J., Cloutis, E., Wang, A., Ruff, S., Craig, M., Bailey, D., Johnson, J., de Souza, P., Farrand, W., 2010. Silica-rich deposits and hydrated minerals at Gusev Crater, Mars: Vis-NIR spectral characterization and regional mapping. Icarus 205, 375–395. https://doi.org/10.1016/j.icarus.2009.03.035.

Rice, M., Bell III, J.F., Arvidson, R., Farrand, W., Johnson, J., Rice Jr., J., Ruff, S.W., Squyres, S.W., Wang, A., 2013a. Mapping hydration with the Mars Exploration Rover (MER) Pancam instruments: recent results from Opportunity at Endeavour crater. In: EGU General Assembly, Vienna, Austria.

Rice, M., Cloutis, E., Bell, J., Bish, D., H, B.H., Mertzman, S., Craig, M., Renaut, R.W., Gautason, B., Mountain, B., 2013b. Reflectance spectra diversity of silica-rich materials: Sensitivity to environment and implications for detections on Mars. Icarus 223, 499–533. https://doi.org/10.1016/j.icarus.2012.09.021.

Rull, F., Maurice, S., Hutchinson, I., Moral, A., Perez, C., Diaz, C., Colombo, M., Belenguer, T., Lopez-Reyes, G., Sansano, A., Forni, O., Parot, Y., Striebig, N., Woodward, S., Howe, C., Tarcea, N., Rodriguez, P., Seoane, L., Santiago, A.,

Rodriguez-Prieto, J.A., Medina, J., Gallego, P., Canchal, R., Santamaría, P., Ramos, G., Vago, J.L., on behalf of the RLS Team, 2017. The Raman laser spectrometer for the ExoMars rover mission to mars. Astrobiology 17, 627–654. https://doi.org/10.1089/ast.2016.1567.

Squyres, S.W., Arvidson, R.E., Ruff, S., Gellert, R., Morris, R.V., Ming, D.W., Crumpler, L., Farmer, J.D., Marais, D.J.D., Yen, A., McLennan, S.M., Calvin, W., Bell, J.F., Clark, B. C., Wang, A., McCoy, T.J., Schmidt, M.E., de Souza, P.A., 2008. Detection of silica-rich deposits on Mars. Science 320, 1063–1067. https://doi.org/10.1126/science.1155429.

Sun, V., Milliken, R., 2018. Distinct geologic settings of opal-A and more crystalline hydrated silica on Mars. Geophys. Res. Lett. 45, 10,221–10,228. https://doi.org/10.1029/2018GL078494.

Tarnas, J., Mustard, J., Lin, H., Goudge, T., Amador, E., Bramble, M., Kremer, C., Zhang, X., Itoh, Y., Parente, M., 2019. Orbital identification of hydrated silica in Jezero crater, Mars. Geophys. Res. Lett. 46, 12,771–12,782. https://doi.org/10.1029/2019GL085584.

The ExoMars 2018 Landing Site Selection Working Group, 2014. Recommendation for the narrowing of ExoMars 2018 Landing sites. Technical Report EXM-SCI-LSS-ESA/IKI-004. European Space Agency.

Vago, J.L., Westall, F., Pasteur Instrument Teams, Landing Site Selection Working Group, Contributors, Other, Coates, A.J., Jaumann, R., Korablev, O., Ciarletti, V., Mitrofanov, I., Josset, J.L., De Sanctis, M.C., Bibring, J.P., Rull, F., Goesmann, F., Steininger, H., Goetz, W., Brinckerhoff, W., Szopa, C., Raulin, F., Westall, F., Edwards, H.G.M., Whyte, L.G., Fairén, A.G., Bibring, J.P., Bridges, J., Hauber, E., Ori, G.G., Werner, S., Loizeau, D., Kuzmin, R.O., Williams, R.M.E., Flahaut, J., Forget, F., Vago, J.L., Rodionov, D., Korablev, O., Svedhem, H., Sefton-Nash, E., Kminek, G., Lorenzoni, L., Joudrier, L., Mikhailov, V., Zashchirinskiy, A., Alexashkin, S., Calantropio, F., Merlo, A., Poulakis, P., Witasse, O., Bayle, O., Bayón, S., Meierhenrich, U., Carter, J., García-Ruiz, J.M., Baglioni, P., Haldemann, A., Ball, A.J., Debus, A., Lindner, R., Haessig, F., Monteiro, D., Trautner, R., Voland, C., Rebeyre, P., Goulty, D., Didot, F., Durrant, S., Zekri, E., Koschny, D., Toni, A., Visentin, G., Zwick, M., van Winnendael, M., Azkarate, M., Carreau, C., the ExoMars Project Team, 2017. Habitability on early Mars and the search for biosignatures with the ExoMars rover. Astrobiology 17, 471–510. https://doi.org/10.1089/ast.2016.1533.

Van Keulen, L., McCord, T., Hansen, G., Hibbitts, C., Crowley, J., 2000. The effect of grain size on the near-infrared reflectance spectra of some hydrated salt minerals. In: Lunar and Planetary Science Conference 31. Abstract 1539.

Vaniman, D.T., Bish, D.L., Ming, D.W., Bristow, T.F., Morris, R.V., Blake, D.F., Chipera, S. J., Morrison, S.M., Treiman, A.H., Rampe, E.B., Rice, M., Achilles, C.N., Grotzinger, J.P., McLennan, S.M., Williams, J., Bell, J.F., Newsom, H.E., Downs, R.T., Maurice, S., Sarrazin, P., Yen, A.S., Morookian, J.M., Farmer, J.D., Stack, K., Milliken, R.E., Ehlmann, B.L., Sumner, D.Y., Berger, G., Crisp, J.A., Hurowitz, J.A.,

Anderson, R., Des Marais, D.J., Stolper, E.M., Edgett, K.S., Gupta, S., Spanovich, N., Science Team, M.S.L., 2014. Mineralogy of a mudstone at Yellowknife Bay, Gale crater, Mars. Science 343. https://doi.org/10.1126/science.1243480.

Venerada, M., Lopez-Reyes, G., Manrique-Martinez, J.A., Sanz-Arranz, A., Lalla, E., Konstantinidis, M., Moral, A., Medina, J., Rull, F., 2020. ExoMars Raman Laser Spectrometer (RLS): development of chemometric tools to classify ultramafic igneous rocks on Mars. Sci. Rep. 10, 16,954. https://doi.org/10.1038/s41598-020-73,846-y.

Viviano-Beck, C.E., Seelos, F.P., Murchie, S.L., Kahn, E.G., Seelos, K.D., Taylor, H.W., Taylor, K., Ehlmann, B.L., Wiseman, S.M., Mustard, J.F., Morgan, M.F., 2014. Revised CRISM spectral parameters and summary products based on the currently detected mineral diversity on Mars. J. Geophys. Res. Planets 119, 1403–1431. https://doi.org/10.1002/2014JE004627.

Wellington, D., Bell III, J., Johnson, J., Kinch, K., Rice, M., Godber, A., Ehlmann, B., Fraeman, A., Hardgrove, C., The MSL Science Team, 2017. Visible to near-infrared MSL/Mastcam multispectral imaging: Initial results from select high-interest science targets within Gale Crater, Mars. Am. Mineral. 102, 1202–1217.

Wiens, R.C., Maurice, S., Barraclough, B., Saccoccio, M., Barkley, W.C., Bell, J.F., Bender, S., Bernardin, J., Blaney, D., Blank, J., Bouyé, M., Bridges, N., Bultman, N., Caïs, P., Clanton, R.C., Clark, B., Clegg, S., Cousin, A., Cremers, D., Cros, A., DeFlores, L., Delapp, D., Dingler, R., D'Uston, C., Darby Dyar, M., Elliott, T., Enemark, D., Fabre, C., Flores, M., Forni, O., Gasnault, O., Hale, T., Hays, C., Herkenhoff, K., Kan, E., Kirkland, L., Kouach, D., Landis, D., Langevin, Y., Lanza, N., LaRocca, F., Lasue, J., Latino, J., Limonadi, D., Lindensmith, C., Little, C., Mangold, N., Manhes, G., Mauchien, P., McKay, C., Miller, E., Mooney, J., Morris, R. V., Morrison, L., Nelson, T., Newsom, H., Ollila, A., Ott, M., Pares, L., Perez, R., Poitrasson, F., Provost, C., Reiter, J.W., Roberts, T., Romero, F., Sautter, V., Salazar, S., Simmonds, J.J., Stiglich, R., Storms, S., Striebig, N., Thocaven, J.J., Trujillo, T., Ulibarri, M., Vaniman, D., Warner, N., Waterbury, R., Whitaker, R., Witt, J., Wong-Swanson, B., 2012. The ChemCam instrument suite on the mars science laboratory (MSL) rover: body unit and combined system tests. Space Sci. Rev. 170, 167–227. https://doi.org/10.1007/s11214-012-9902-4.

Wu, C.Y., Jacobson, A., Laba, M., Baveye, P., 2009. Alleviating moisture content effects on the visible near-infrared diffuse-reflectance sensing of soils. Soil Sci. 174, 456–465. https://doi.org/10.1097/SS.0b013e3181b21491.

Yen, A.S., Gellert, R., Schröder, C., Morris, R.V., Bell, J.F., Knudson, A.T., Clark, B.C., Ming, D.W., Crisp, J.A., Arvidson, R.E., Blaney, D., Brückner, J., Christensen, P.R., DesMarais, D.J., de Souza, P.A., Economou, T.E., Ghosh, A., Hahn, B.C., Herkenhoff, K.E., Haskin, L.A., Hurowitz, J.A., Joliff, B.L., Johnson, J.R., Klingelhöfer, G., Madsen, M.B., McLennan, S.M., McSween, H.Y., Richter, L., Rieder, R., Rodionov, D., Soderblom, L., Squyres, S.W., Tosca, N.J., Wang, A., Wyatt, M., Zipfel, J., 2005. An integrated view of the chemistry and mineralogy of martian soils. Nature 436, 49–54. https://doi.org/10.1038/nature03637.